Article
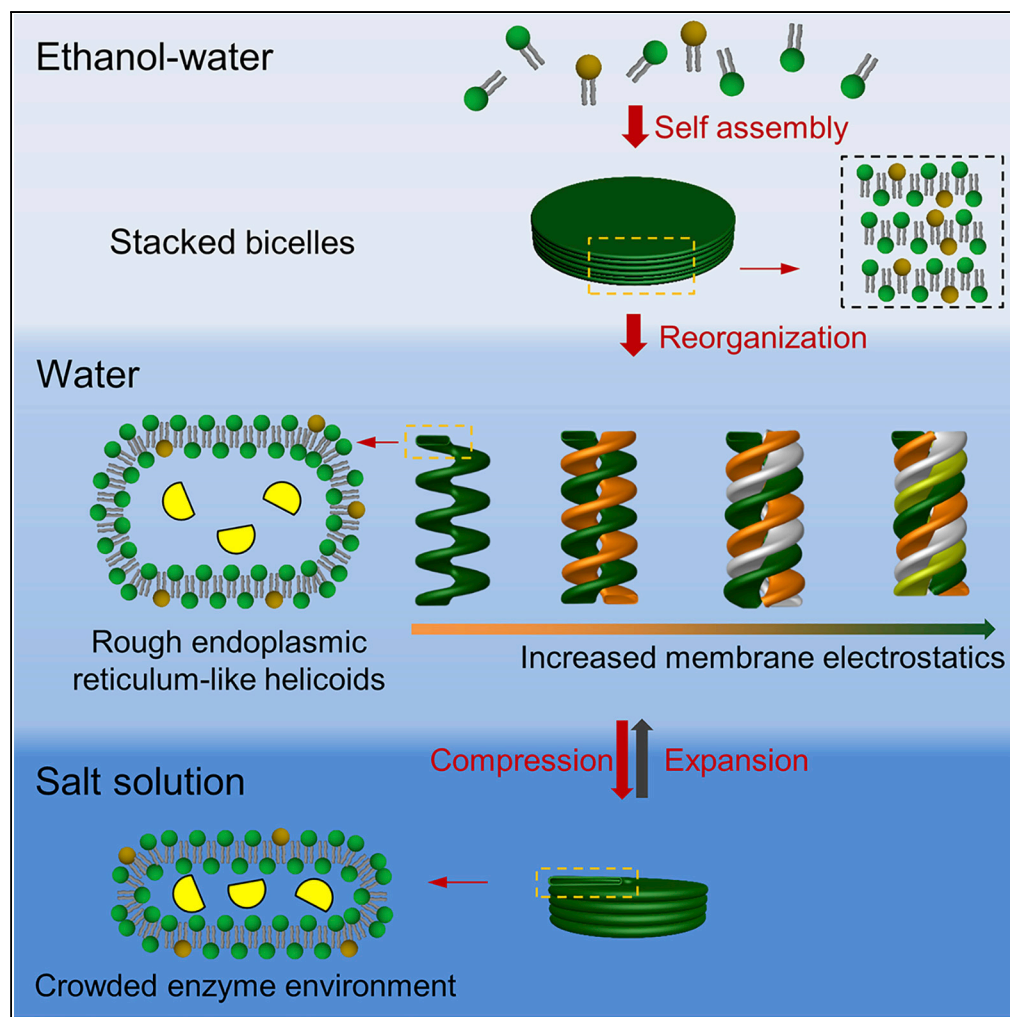
Self-Assembled Rough Endoplasmic Reticulum-Like Proto-Organelles

Qingchuan Li,
Xiaojun Han

hanxiaojun@hit.edu.cn

HIGHLIGHTS

Rough endoplasmic reticulum-like helicoids were formed from phospholipids

Membrane electrostatics controls helicoids formation and probably organelle shaping

The helicoids reversibly expand and compress to control loaded molecule concentration

A "breathing" modulated proto-organelle model is proposed based on the helicoids

Article

Self-Assembled Rough Endoplasmic Reticulum-Like Proto-Organelles

Qingchuan Li[1] and Xiaojun Han[1,2,*]

SUMMARY

Nature has evolved elaborate, dynamic organelle morphologies for optimal organelle functions. Among them, cisternae stacks are the universal structure for most organelles. However, compared with the well-studied spherical cell/organelle membrane mimic, the fabrication of the ubiquitously present cisternal organelle-like membrane structures for organelle mimic remains a challenging task. Herein, rough endoplasmic reticulum (RER)-like helicoidal cisternae stacks were assembled to mimic the enzyme crowded environment in spatially confined RER cisternae. RER-like single helicoid, multiple helicoids, and secondary helix are all observed. Membrane electrostatics drives their formation and controls the percentages, which indicates the possible role of membrane electrostatics in RER shaping. The organelle-like cisternae stacks can reversibly expand and compress, which provides modulated crowded or de-crowded enzyme environment for biochemical reactions. This work provides advanced membrane models, and novel mechanisms for organelle shaping and helicoids formation, and holds great potential in biomimetics, cell biology, and advanced materials design.

INTRODUCTION

The existence of diverse intracellular membrane systems with characteristic morphologies was one of the most fascinating features of eukaryotic cells. Among them, cisternae stacks extensively found in Golgi apparatus, grana, and rough endoplasmic reticulum (RER) constituted the major component of intracellular membrane systems. However, although they shared similar cisternae-stacks-based morphologies, these intracellular membrane systems were essentially different in their spatial organization. The cisternae stacks in Golgi apparatus stacked close to each other via protein connection at a typical intercisternal distance of 7–15 nm (Tachikawa and Mochizuki, 2017; Mollenhauer and Morré, 1991). The grana existed as cylindrical stacks of flattened and closely appressed cisternae, which were interconnected by the fret-like stromal lamellae around the cylinder (Ruban and Johnson, 2015; Shimoni et al., 2005). On the contrary, the RER was recently discovered to be composed of a structural motif of helicoidal cisternae stacks resembling spiral stairs to form continuous membrane system (Terasaki et al., 2013). The mechanisms for the generation and maintenance of these different cisternae-stacks-based intracellular membrane systems are still less understood.

Artificial membranes provided simplified models for studying and emulating biological membrane systems. In the past decades, scientists have developed a variety of model systems, including vesicles (Deshpande et al., 2016), tubes (Bi et al., 2014), supported or suspended lipid bilayers (Tayebi et al., 2012; Osaki and Takeuchi, 2017; Fuhs et al., 2018), bicelles (Dürr et al., 2012), and nanodisks (Ravula et al., 2017). To further mimic the complexity of natural membrane systems, more complex membrane structures including multilamellar (Matosevic and Paegel, 2013) and multicompartmented vesicles (Zong et al., 2017; Deng et al., 2017), stacked bicelles or nanodisks (Matsui et al., 2015; Yang et al., 2014; Wang et al., 2018), and tube networks/stacks (Karlsson et al., 2001; Powers et al., 2017; Zhang et al., 2017) were recently developed. These artificial membrane systems supplied platforms for the study of protein structures and functions (Dürr et al., 2012; Zhang et al., 2016; Burré et al., 2010), the investigation of cellular processes (Fenz et al., 2017; Kamiya et al., 2016; Küchler et al., 2016), and biomimetics (Li and Han, 2018; Altamura et al., 2017; Adamala et al., 2016; Heath et al., 2017; Park et al., 2018), and provided important clues for membrane shaping (Powers et al., 2017; Shi and Baumgart, 2015). However, cisternae stacks, especially the helicoidal structures found in RER, were rarely artificially fabricated from phospholipids.

Herein, stacked bicelles incorporated with charged lipids were assembled in ethanol-water solution via a recrystallization process. When suspended in water, they quickly transformed to RER-like helicoidal

[1]State Key Laboratory of Urban Water Resource and Environment, School of Chemistry and Chemical Engineering, Harbin Institute of Technology, 92 West Da-Zhi Street, Harbin 150001, China

[2]Lead Contact
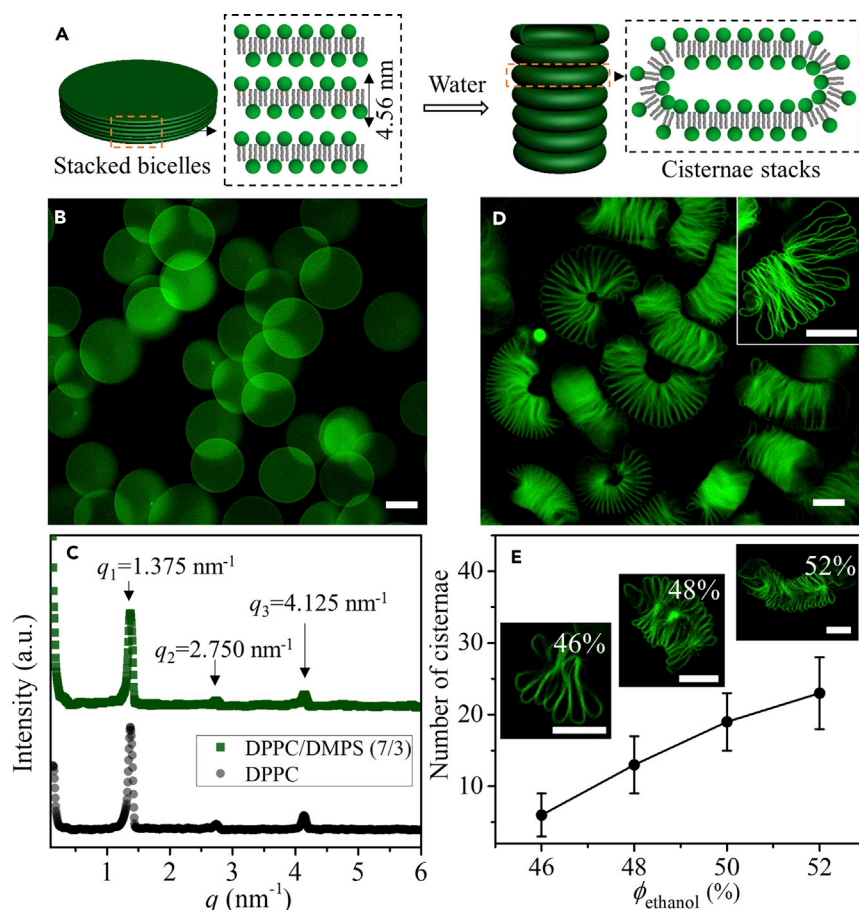
*Correspondence: hanxiaojun@hit.edu.cn

Figure 1. Cisternae Stacks Formation from Micro-Sized Stacked Bicelles

(A) Schematic illustration of the transformation of stacked bicelles to cisternae stacks in water.

(B) Fluorescence image of stacked bicelles formed in 50% ethanol solution.

(C) SAXS profiles of stacked bicelles formed in 50% ethanol solution with different phospholipid compositions.

(D) Fluorescence image of cisternae stacks transformed from stacked bicelles formed in 50% ethanol solution. The inset is the confocal fluorescence image of one cisternae stack.

(E) Variation of the number of cisternae in cisternae stacks with ethanol volume percentage $\Phi_{ethanol}$ (N = 200). The insets are typical confocal fluorescence images. Phospholipid concentration of 0.10 mg/mL was used in these experiments. Scale bars, 10 μm. Error bars are ± SEM. See also Figures S1–S6.

cisternae stacks, which can further spiral to secondary helical structures. The influences of the parameters for stacked bicelles formation and reorganization were investigated to reveal the mechanisms for the formation of helicoidal cisternae stacks. Biomolecules such as fluorescent polymers or enzymes in the cisternae stacks can be reversibly concentrated and diluted for crowding of molecules. The formation of helicoidal cisternae stacks with encapsulated biomolecules provided RER-like proto-organelle models to study or mimic their functions and clues for the mechanisms of helicoidal structure formation in cells.

RESULTS AND DISCUSSION

Cisternae Stacks Formation Composed of Continuous Membrane Systems

Micro-sized stacked bicelles were formed from negatively charged 1,2-dipalmitoyl-*sn*-glycero-3-phospho-choline (DPPC)/1,2-dimyristoyl-*sn*-glycero-3-phospho-L -serine (sodium salt) (DMPS) (*w/w*, 7/3) mixtures by slowly cooling the phospholipid dissolved in 50% ethanol-water solution from 50°C to 25°C at a rate of 0.5°C/min (Figures 1A–1C). Similar to the results from zwitterionic DPPC (Li and Han, 2018), stacked bicelles from DPPC/DMPS (*w/w*, 7/3) were formed in a well-defined round shape with an average diameter of ~15 μm, as depicted by the fluorescence image (Figure 1B). The small-angle X-ray scattering (SAXS)

profiles of the stacked bicelles displayed only one set of lamellar diffraction peaks, at $q_1 = 1.375$ nm^{-1}, $q_2 = 2.750$ nm^{-1}, and $q_3 = 4.125$ nm^{-1} (Figure 1C), which confirmed the periodic lamellar structure of the stacked bicelles with periodic spacing d of 4.56 nm, as given by $d = 2\pi/q_1$. The periodic spacing of 4.56 nm included the thickness of lipid membrane and the thickness of solvent layer, which indicated the interdigitated phase in the bicelles (Adachi et al., 1995). The incorporation of negatively charged DMPS displayed no influence on the periodic spacing from the SAXS profiles (Figure 1C), which might be due to the screening of the repulsive forces among lipid bilayers in the ethanol-water solvent condition with relative lower dielectric constant. However, the existence of DMPS slightly decreased the main phase transition temperature T_m according to the differential scanning calorimetry results (Figure S1), from 40.2°C for DPPC bicelles to 39.4°C for DPPC/DMPS bicelles.

When dispersed in water or ethanol-water solution with ethanol volume percentage $\Phi_{ethanol}$ below 20%, the increased edge energy and reanimated electrostatic repulsive energy drove the prompt transformation of stacked bicelles to cisternae stacks in seconds after a short delay (Figures S2 and S3). These cisternae stacks with cisternae piled one by one can be clearly recognized from the fluorescence images (Figures 1D and S3). Water-soluble fluorescent markers Rhodamine B isothiocyanate-Dextran (~70 kDa) were entrapped in the cisternae stacks during the reorganization process (Figure S4), which indicated the separated phase of the cisternae stacks from outer solution. The number of cisternae in the cisternae stacks can be modulated from ~5 to ~20 by the variation of $\Phi_{ethanol}$ for stacked bicelles formation (Figures 1E and S5). With increased $\Phi_{ethanol}$, cisternae stacks with more cisternae formed. The percentage of negatively charged DMPS had no obvious influence on the number of cisternae in the cisternae stacks (Figure S6).

Confirmation of the Formation of RER-Like Helicoids and Multiple Helicoids

The cisternae stacks can maintain their morphology for at least 1 month at 25°C. However, when treated with heating or shaking, they paved different morphology evolution pathways (Figure S7), including spatially segmented multilamellar vesicles (Figure S7D), erythrocyte (Figure S7E). After heating at 35°C (below phase transition temperature T_m of 39.4°C) for about 12 hr, some of the cisternae stacks fully expanded and formed continuous membranes, such as randomly curved complete membranes or helix (Figure S7B), which indicated that the cisternae in the stacks might be physically connected to form continuous membrane systems. To identify how they were connected, fluorescence images of the cisternae stacks in z stacks at 0.32 μm were taken to construct the 3D structures of the cisternae stacks (Figure 2). Most of the cisternae stacks were proved to be in helicoidal structures with different number of helicoids n in one cisternae stack, including RER-like single helicoids ($n = 1$) (Figure 2) and multiple helicoids such as double ($n = 2$, Figure 3A), triple ($n = 3$, Figure 3B), quad ($n = 4$, Figure 3C), penta ($n = 5$, Figure S8), and hexa helicoids ($n = 6$, Figure S8). Single helicoidal cisternae stacks were previously reported to be the structural motif of RER in cells, where the right- and left-handed helicoids were alternatively connected to form continuous membrane systems (Figure 2A). In our work, both right- and left-handed helicoids were found. The confocal fluorescence images in z stacks (obtained from top to bottom) provided primitive evidence to quickly identify the chirality of the helicoids (Figures 2B–2D). As indicated by the yellow dashed arrows in Figures 2B and 2C and the schematic in Figure 2D, the cisternae in the stack were piled one by one with no obvious connections in panel 1. In subsequent panels (panels 2 and 3 in Figure 2B, panels 3 and 4 in Figure 2C, and panels 2 and 3 in Figure 2D), each cisterna disconnected into two parts. In the next set of panels, one part of the disconnected cisternae connected with the opposite part of neighboring cisternae depending on the chirality. For right-handed helicoids, the left part of a disconnected cisterna s tended to subsequently connect with the right part of another disconnected cisterna $s+1$. For example, the left part of cisternae I, II, and III connected with the right part of cisternae II, III, and IV, respectively, as indicated by the yellow dashed arrows in panel 6 in Figure 2B. On the contrary, for left-handed helicoids, the right part of cisterna s connected with left part of cisterna $s+1$ (panel 6 in Figure 2C and panel 4 in Figure 2D). The 3D reconstruction of the cisternae stack (middle in Figure 2E and Video S1) illustrated that the cisternae stack possessed twisted surface that has a handedness, forming a continuous membrane system. To view the spiral stair structure more clearly, 3D structure of the cisternae stack along the midline (yellow dashed lines and arrows in Figures 2B and 2C) of the cisternae was reconstructed (right in Figure 2E and Video S2), which further reinforced that the membrane twisted as helicoids resembling spiral stairs, similar to the structural motif of RER. The ratio of right- and left-handed RER-like cisternae stacks was counted to be approximately 1:1, independent of $\Phi_{ethanol}$ (Figure 2F). In RER, the right- and left-handed connections shared the same ratio (Marshall, 2013).
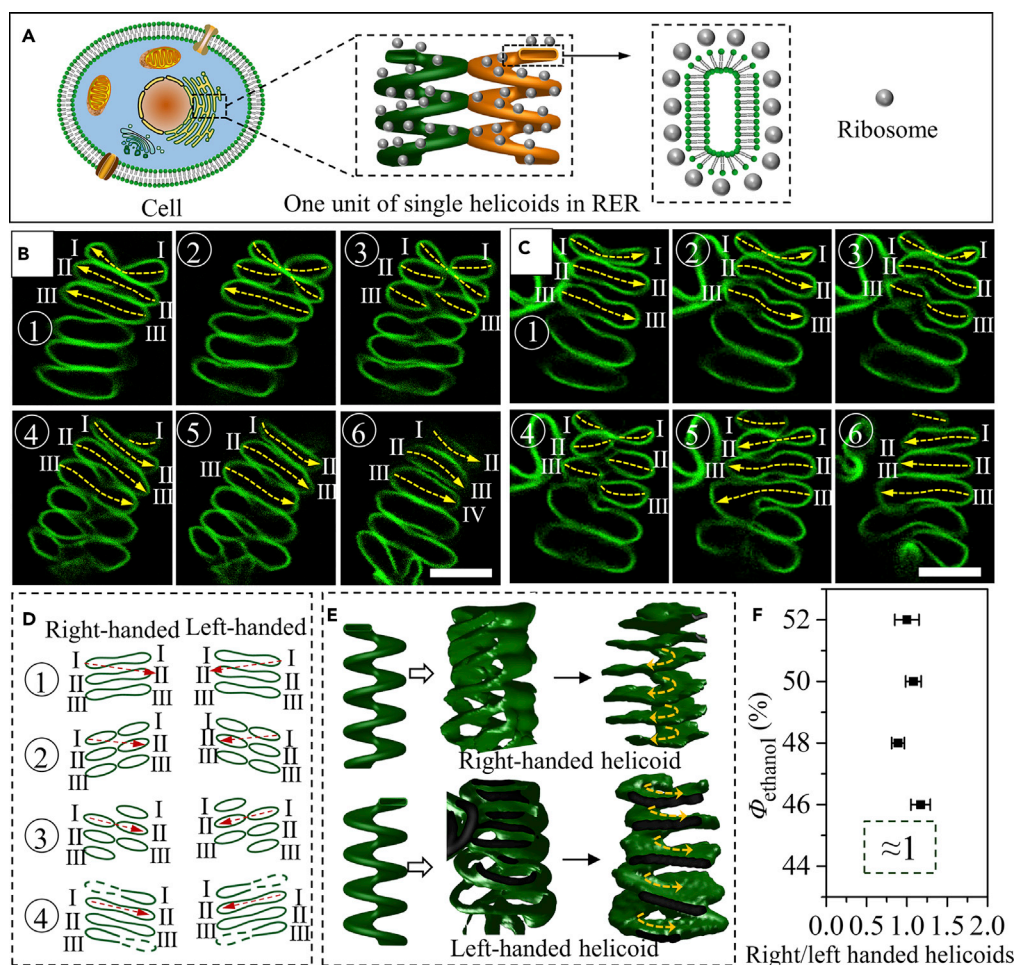
Figure 2. Formation of RER-Like Single Helicoidal Cisternae Stacks

(A) Schematic illustration of RER in cells.

(B and C) Typical fluorescence images of the right-handed (B) and left-handed (C) RER-like helicoids visualized in z-stacks by laser confocal microscopy. The yellow dash arrows indicate the midline of the cisternae.

(D) Schematic illustration of variation of the cisternae in z stacks under laser confocal fluorescence microscopy for cisternae stacks with different chirality. The red dash arrows indicate that there exist connections between two cisternae.

(E) The 3D reconstruction of the z stacks in (B) and (C) (middle) or the midline of the cisternae (right). The yellow dashed arrows indicate the spiral directions of the helicoids.

(F) Counted ratio of right- to left-handed stacks formed in solution with different $\Phi_{ethanol}$.

Scale bars, 10 μm. Error bars are ±SEM. See also Figure S7.

In addition to the above demonstrated RER-like single helicoidal shape, cisternae stacks composed of multiple helicoids with two or more helicoids in one cisternae stack were also observed (Figures 3 and S8). Figures 3A–3C presented typical fluorescence images from the z stacks for the reconstruction of double, triple, and quad helicoidal membrane structures, respectively. Similar to the condition for single helicoid, the cisternae in the images with small panel numbers piled shoulder by shoulder (panel 1 in Figures 3A–3C), and then disconnected with the increase in panel numbers (panels 3 and 4 in Figures 3A–3C). The difference was, in the subsequent panel numbers, the disconnected cisternae (s) in one side failed to connect with the opposite part of the neighboring cisternae (s+1) as the case for single helicoid (Figure 2D), but connected to those cisternae with an interval of one cisterna (double helicoid in Figure 3A, where the left part of cisterna I connected with the right part of cisterna III as seen in panel 5), two cisternae (triple helicoid in Figure 3B, where the left part of cisterna I connected with the right part of cisterna IV as seen in panel 6), three cisternae (quad helicoid in Figure 3C, where the left part of cisterna I connected with the right part of cisterna V as seen in panel 6), four cisternae (penta helicoid in Figure S8), or five cisternae (hexa helicoid in Figure S8). In brief, for a multiple helicoidal structure with *n* helicoids, an interval
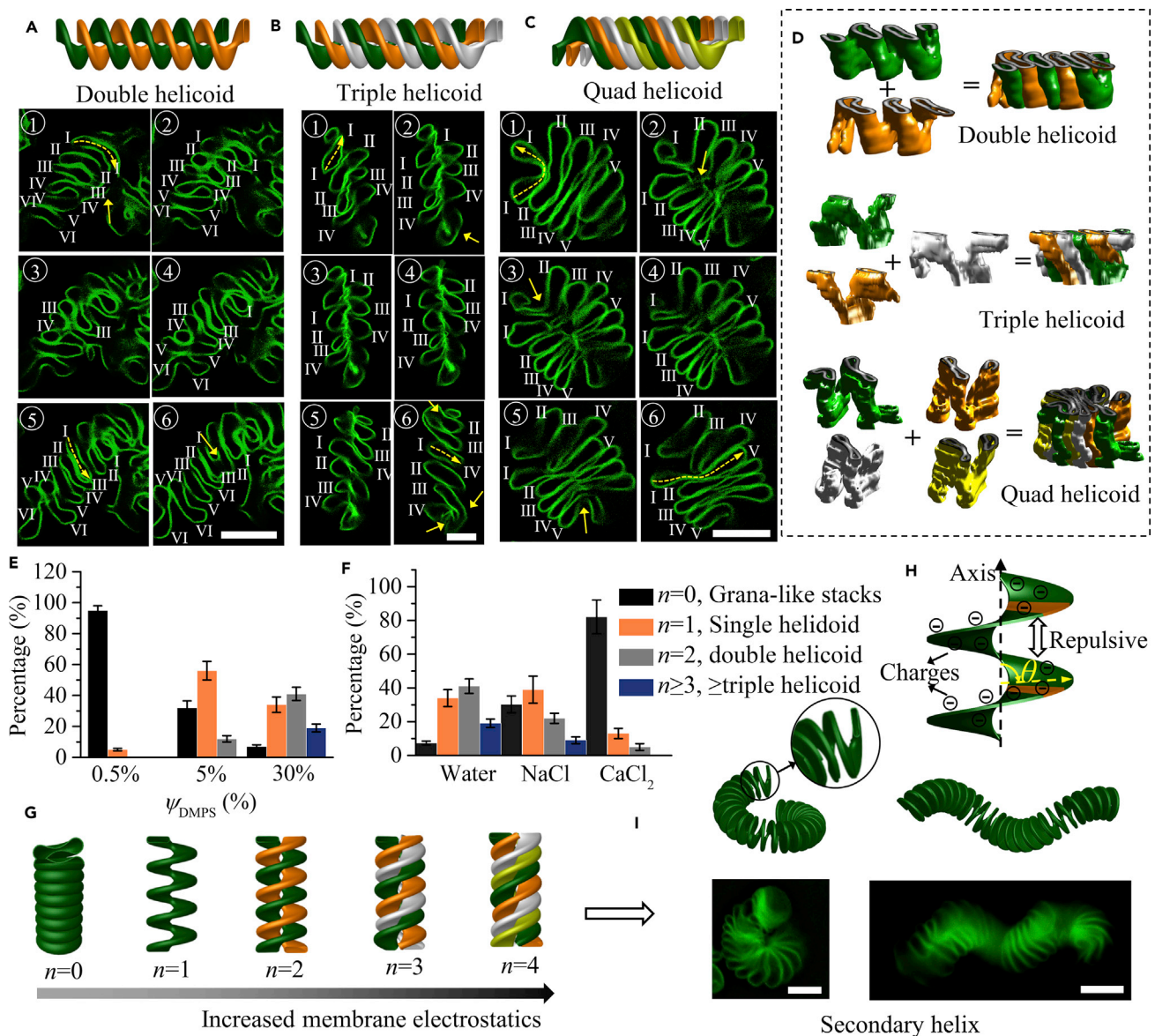
Figure 3. Formation of Multiple Helicoidal Cisternae Stacks and Secondary Helix

(A–C) Schematic illustration and typical fluorescence images of the multiple helicoids visualized in z stacks of double (A), triple (B), and quad (C) helicoidal cisternae stacks.

(D) 3D reconstruction of the multiple helicoidal cisternae stacks. Different helicoids in one cisternae stack were painted with different colors.

(E) Influence of the percentage of negatively charged DMPS ψ_{DMPS} in DPPC/DMPS stacked bicelles on the percentages of cisternae stacks with different n (N = 100).

(F) Variation of the percentages of helicoidal cisternae stacks (containing 30% DMPS) with different n when ions were added to screen the electrostatic repulsive forces during the reorganization process (N = 100). The stacked bicelles were formed in 50% ethanol solution and then dispersed into water to obtain cisternae stacks.

(G) Schematic illustration of the influences of charged lipids on the formation of cisternae stacks with different n.

(H) Schematic representation of a helicoid with angle of θ between the axis and local ramp plane. The orange surfaces indicated two parallel planes in the helicoid that repelled each other under electrostatic repulsive force.

(I) The schematic and fluorescence images for the formation of secondary helix from the helicoidal cisternae stacks.

Scale bars, 10 μm. Error bars are ±SEM. See also Figures S8–S19.

of n-1 cisternae can be observed between two connected cisternae (Figure S9), the validity of which was further verified by the perfect reproduction of the observed experimental results in the serial sections of real helicoidal models (Figure S10). The morphology of the cisternae stacks with multiple helicoidal

structural motifs was clearly illustrated from the 3D reconstructions in Figure 3D and Video S3. The helicoids in one cisternae stack were also connected with each other to form continuous membrane systems with interconnected single lumens, as indicated by the solid yellow arrows in Figures 3A–3C.

Helicoids Formation Mechanisms

For samples incorporated with 30% DMPS, when water (25°C) was used for the reorganization of stacked bicelles ($\Phi_{ethanol}$ = 50% for the formation) to cisternae stacks, the average percentages of cisternae stacks with different n were 6% (n = 0, grana-like cisternae stacks), 34% (n = 1), 41% (n = 2), and 19% ($n \geq$ 3), respectively (Figure 3E). However, if the conditions for stacked bicelles formation or their reorganization to cisternae stacks were changed, the percentages can be varied (Figures 3E, 3F, and S11–S15). From the statistical analysis of the cisternae stacks samples formed at different conditions, we established the contribution of increased membrane electrostatics and decreased membrane bending elasticity to drive the formation of helicoidal cisternae stacks with increased n. With regard to membrane bending elasticity, higher temperature of the reorganization process that can soften lipid bilayers resulted in relatively larger n (Figure S11A), whereas the incorporation of phospholipids that can stiffen membranes (Figure S12), such as negatively charged 1,2-dipalmitoyl-sn-glycero-3-phospho-(1'-rac-glycerol) (sodium salt) or zwitterionic 1,2-distearoyl-sn-glycero-3-phosphocholine, caused smaller n. With regard to membrane electrostatics, parameters that cause the accumulation of electrostatic repulsive energy, such as increased percentages of negatively charged DMPS (Figures 3E and S13) or positively charged 1,2-di-(9Z-octadecenoyl)-3-trimethylammonium-propane (chloride salt) (Figure S14) resulted in larger n, whereas solvent conditions of NaCl solution, $CaCl_2$ solution, or ethanol-water mixture that can screen electrostatic forces resulted in smaller n (Figure 3F). The electrostatics can also be readily altered by simply changing the solution pH. The average n initially decreased with the solution pH value from 7.0 to 3.6, and then increased from 3.6 to 2.0 (Figure S15). Minimum n was obtained at pH = 3.6, around the isoelectric point of phosphocholine (PC)-phosphatidylserine (PS) membrane system (Naumowicz and Figaszewski, 2014), which confirmed the important role of membrane electrostatics in forming helicoids. The ethanol volume percentage $\Phi_{ethanol}$ of the ethanol-water solution for bicelles formation also influenced the percentages of different morphologies in the cisternae stacks. With higher $\Phi_{ethanol}$, the average n increased (Figure S16) due to the following two reasons. First, with increased $\Phi_{ethanol}$, more ethanol molecules were incorporated in the lipid assemblies (Ly and Longo, 2004; Vanegas et al., 2010), which softened the lipid bilayer to facilitate their morphology transformation. Second, with increased $\Phi_{ethanol}$, thicker bicelles were formed, which caused more accumulated electrostatic repulsive force to drive the transformation of bicelles to cisternae stacks with increased n (Figure S17).

Taken together, membrane electrostatics drove the formation of helicoidal cisternae stacks with increased n against the resistance of membrane bending elasticity to deform the membranes (Figure 3E). The decreased electrostatic repulsive energy W_e of helicoidal structures might be responsible for the formation of helicoids with different n. For two parallel surfaces in the helicoid with angle θ between the axis and local ramp plane (Figure 3F), W_e was given as $W_e = -\int_{\infty}^{Z} P(Z)d_Z$, where z was the distance between the two surfaces and $P(z)$ was the lateral pressure expressed as $P(Z) = 2\varepsilon_0\varepsilon_s K^2(kT/e)^2 sin(\theta)$, with ε_0, ε_s, k, T e, and K, respectively, representing dielectric constant of vacuum, dielectric constant of solvent, Boltzmann constant, temperature, elementary electron charge, and a parameter related to charge density (Israelachvili, 2015). With the decrease of θ, $P(z)$ decreased, so smaller W_e was obtained. Therefore, flat surface (θ = 90°) tended to transform to helicoid (θ < 90°) to decrease W_e. The formation of multiple helicoids might be related to the transient volume-confined state at the sudden variation of solvent condition. Obviously, with fixed number of lipid bilayers in fixed confined space, multiple helicoids tended to form to achieve smaller θ, namely, more tilted ramps, for lowest W_e. To further decrease the electrostatic energy, secondary helical structures tended to form (Figure 3G), mainly from long and fully expanded helicoidal cisternae stacks, which were easier to twist compared with cisternae stacks with smaller expansion extent. The reorganization of stacked bicelles to helicoidal cisternae stacks might occur in three stages (Figure S18): the fusion of lipid bilayers to form cisternae driven by edge energy (stage 1), the breaking of cisternae to fragmented small helicoids (stage 2), and the fusion of fragmented helicoids to form continuous helicoidal cisternae stacks (stage 3). These three stages might also happen simultaneously.

Charged lipids were the constitutive components of cellular membranes. In RER, the anionic phospholipids such as PS and phosphatidylinositol constituted over 10% of the total lipids (Mato, 1990; van Meer et al.,
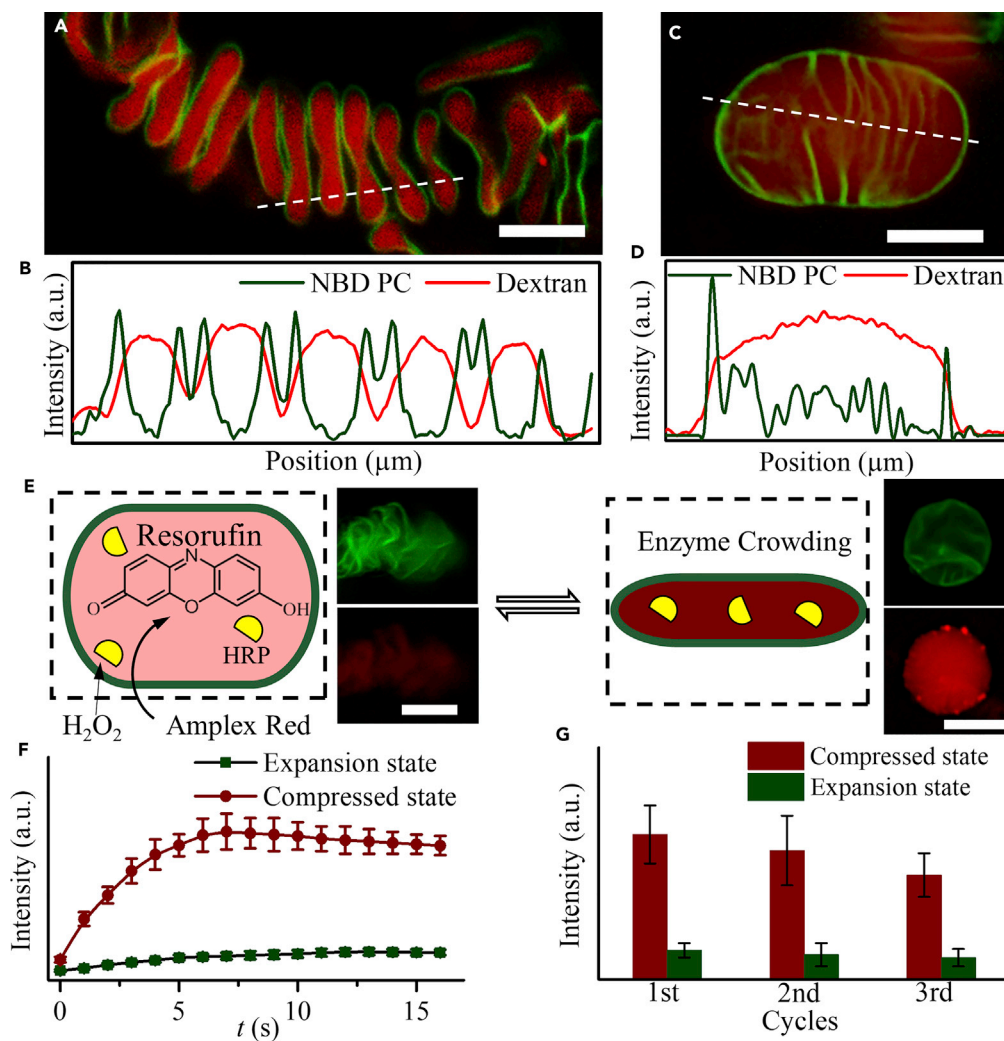
Figure 4. Breathing" Modulated Enzyme Catalytic Process in the Helicoidal Cisternae Stacks

(A and C) Fluorescence image of the helicoidal cisternae stack (A) and ellipsoidal liposome (C) encapsulated with Rhodamine B isothiocyanate-Dextran (~70 kDa).

(B and D) The profile of the fluorescence intensity along the (B) white dashed line in (A) and (D) white dashed line in (C).

(E) Schematic illustration of the enzyme catalytic reactions in the helicoidal cisternae stacks and typical fluorescence images of the cisternae stacks in different states encapsulated with fluorescent products.

(F) Variation of the fluorescence intensity of the fluorescent product resorufin with time for cisternae stacks in expansion state (green curve) and compressed state (red curve), respectively.

(G) Variation of the maximum fluorescence intensity of the reaction product resorufin with cycle numbers in compressed (red) and expanded (green) cisternae stacks.

Scale bars, 10 μm. Error bars are ±SEM. See also Figures S20–S22.

2008). Moreover, the RER sheets were often spatially confined by the cytoplasmic matrix. According to our experimental and calculation results, RER in cells might be helicoidally arranged to decrease interbilayer electrostatic repulsive energy in confined space. Moreover, although not yet reported in RER, multiple helicoids might exist in cells (Figure S19).

Modulated Enzyme Crowding and De-crowding in "Breathing" Cisternae Stacks

The entrapment of biomolecules during the reorganization process demonstrated quite low loading efficiency of molecules (Figure S4) because of the quick reorganization process from bicelles to cisternae stacks. To functionalize the helicoidal cisternae stacks for potential proto-organelle models, a method for high loading efficiency of molecules was desired. Here, we proposed a way for loading of molecules through

the transient membrane defects generated in an exocytosis-like process, mimicking the active secretion process in RER, caused by the binding of free avidin to the cisternae stacks incorporated with 1,2-dipalmitoyl-sn-glycero-3-phosphoethanolamine -N-(cap biotinyl) (sodium salt) (16:0 Biotinyl Cap PE) (Figure S20). The concentration of avidin influenced the loading efficiency and the morphology of the cisternae stacks. When C_{avidin} was below 0.02 mg/mL, the increase of C_{avidin} resulted in the encapsulation of more fluorescent molecules, without influencing the helicoidal structure of the cisternae stacks (Figure S21). However, when C_{avidin} was above 0.05 mg/mL, the cisternae in the stacks fused shoulder by shoulder, forming ellipsoidal liposomes with interconnected inner membrane system, similar to the morphology of some kinds of mitochondria. According to the fluorescence images and fluorescence intensity profiles, the fluorescent molecules were uniformly distributed in the cisternae stacks or ellipsoidal liposomes (Figures 4A–4D). No obvious leakage of fluorescent molecules was observed after several days. The detached "exosomes" encapsulated with high concentration of fluorescent molecules during the exocytosis-like process were observed as red spots sitting on the membrane surface or aggregates in solution (Figures S20B and S20C).

The stacked cisternal structures in cells often displayed "breathing"-like expansion and compression for specific functions. The RER-like helicoidal structures can also "breathe" under the stimuli of external solvent condition (Figure S22). In 150 mM PBS, the cisternae stacks compressed to densely packed membranes with rough surface because of the screening of interbilayer electrostatic repulsive forces, and consequently, fluorescent molecules in them were concentrated. When re-dispersed in water, they restored to loosely packed state, with re-diluted fluorescent molecules. The interbilayer forces (van der Waals force, hydration force, and electrostatic repulsive force) among lipid bilayers and osmotic force were the main driving force for the "breathing." Motivated by the "breathing" property of the cisternae stacks to concentrate or dilute molecules, an adaptive proto-organelle model from external solvent condition was proposed by trapping horseradish peroxidase in the cisternae stacks (Figure 4E). Several seconds after the addition of H_2O_2 and Amplex Red, the typical red fluorescence of resorufin (reaction product) was monitored under the fluorescence microscope (Figure 4E), both for expanded cisternae stacks in water and compressed cisternae stacks in PBS. Because of the relatively concentrated enzyme environment compared with expanded cisternae stacks, quicker increase of fluorescence intensity to higher fluorescence level was observed in cisternae stacks in compressed state (Figure 4F). At least three cycles of luminal-space-modulated enzyme catalytic processes were realized in the "breathing" cisternae stacks, with slight decrease in the measured fluorescence intensities with increased cycle numbers (Figure 4G). In cells, for higher efficiency and better timeliness, most enzyme-catalyzed reactions occurred in molecularly crowded or confined environments. The helicoidal cisternae stacks with "breathing" lumens here can provide robust model to study these enzyme catalytic reactions, especially in some sophisticated systems involving cascade reactions.

In summary, we formed RER-like helicoidal cisternae stacks from charged stacked bicelles and proposed an adaptive proto-organelle model for molecules crowding. Membrane electrostatics controlled the formation of helicoidal cisternae stacks with different n to decrease the electrostatic repulsive energy among lipid bilayers, which might be the possible shaping mechanism for the helicoidal RER in cells. The RER-like cisternae stacks can reversibly expand and compress, which endowed them the ability to be applied in many volume-confined processes. Moreover, except for RER-like helicoidal cisternae stacks, many other novel and advanced membrane models were also provided. This work provided possible organelle shaping mechanisms and advanced membrane models for biomimetics or cell biology.

Limitation of Study

The helicoidal cisternae stacks samples were mixtures of lipid assemblies with different morphologies. Although the percentages can be easily modulated, it is still difficult to form samples with one morphology.

METHODS

All methods can be found in the accompanying Transparent Methods supplemental file.

SUPPLEMENTAL INFORMATION

Supplemental Information includes Transparent Methods, 22 figures, and 3 videos and can be found with this article online at https://doi.org/10.1016/j.isci.2018.09.020.

iScience

CellPress

REFERENCES

Adachi, T., Takahashi, H., Ohki, K., and Hatta, I. (1995). Interdigitated structure of phospholipid-alcohol systems studied by x-ray-diffraction. Biophys. J. 68, 1850–1855.

Adamala, K.P., Martin-Alarcon, D.A., Guthrie-Honea, K.R., and Boyden, E.S. (2016). Engineering genetic circuit interactions within and between synthetic minimal cells. Nat. Chem. 9, 431–439.

Altamura, E., Milano, F., Tangorra, R.R., Trotta, M., Omar, O.H., Stano, P., and Mavelli, F. (2017). Highly oriented photosynthetic reaction centers generate a proton gradient in synthetic protocells. Proc. Natl. Acad. Sci. U S A 114, 3837–3842.

Bi, H., Fu, D., Wang, L., and Han, X. (2014). Lipid nanotube formation using space-regulated electric field above interdigitated electrodes. ACS Nano 8, 3961–3969.

Burré, J., Sharma, M., Tsetsenis, T., Buchman, V., Etherton, M.R., and Südhof, T.C. (2010). α-Synuclein promotes SNARE-complex assembly in vivo and in vitro. Science 329, 1663–1667.

Dürr, U.H., Gildenberg, M., and Ramamoorthy, A. (2012). The magic of bicelles lights up membrane protein structure. Chem. Rev. 112, 6054–6074.

Deng, N.N., Yelleswarapu, M., Zheng, L., and Huck, W.T.S. (2017). Microfluidic assembly of monodisperse vesosomes as artificial cell models. J. Am. Chem. Soc. 139, 587–590.

Deshpande, S., Caspi, Y., Meijering, A.E.C., and Dekker, C. (2016). Octanol-assisted liposome assembly on chip. Nat. Commun. 7, 10447.

Fenz, S.F., Bihr, T., Schmidt, D., Merkel, R., Seifert, U., Sengupta, K., and Smith, A.-S. (2017). Membrane fluctuations mediate lateral interaction between cadherin bonds. Nat. Phys. 13, 906–913.

Fuhs, T., Klausen, L.H., Sonderskov, S.M., Han, X., and Dong, M. (2018). Direct measurement of surface charge distribution in phase separating supported lipid bilayers. Nanoscale 10, 4538–4544.

Heath, G.R., Li, M., Rong, H., Radu, V., Frielingsdorf, S., Lenz, O., Butt, J.N., and Jeuken, L.J.C. (2017). Multilayered lipid membrane stacks for biocatalysis using membrane enzymes. Adv. Funct. Mater. 27, 1606265.

Israelachvili, J.N. (2015). Intermolecular and Surface Forces (Academic press).

Küchler, A., Yoshimoto, M., Luginbühl, S., Mavelli, F., and Walde, P. (2016). Enzymatic reactions in confined environments. Nat. Nanotechnol. 11, 409–420.

Kamiya, K., Kawano, R., Osaki, T., Akiyoshi, K., and Takeuchi, S. (2016). Cell-sized asymmetric lipid vesicles facilitate the investigation of asymmetric membranes. Nat. Chem. 8, 881–889.

Karlsson, A., Karlsson, R., Karlsson, M., Cans, A.-S., Strömberg, A., Ryttsén, F., and Orwar, O. (2001). Networks of nanotubes and containers. Nature 409, 150–152.

Li, Q., and Han, X. (2018). Self-assembled "breathing" grana-like cisternae stacks. Adv. Mater. 30, 1707482.

Ly, H.V., and Longo, M.L. (2004). The influence of short-chain alcohols on interfacial tension, mechanical properties, area/molecule, and permeability of fluid lipid bilayers. Biophys. J. 87, 1013–1033.

Marshall, W.F. (2013). Differential geometry meets the cell. Cell 154, 265–266.

Mato, J.M. (1990). Phospholipid Metabolism in Cellular Signaling (CRC Press).

Matosevic, S., and Paegel, B.M. (2013). Layer-by-layer cell membrane assembly. Nat. Chem. 5, 958–963.

Matsui, R., Ohtani, M., Yamada, K., Hikima, T., Takata, P.M., Nakamura, T., Koshino, H., Ishida, Y., and Aida, P.T. (2015). Chemically locked bicelles with high thermal and kinetic stability. Angew. Chem. Int. Ed. 54, 13284–13288.

Mollenhauer, H.H., and Morré, D.J. (1991). Perspectives on Golgi apparatus form and function. J. Electron Microsc. Tech. 17, 2–14.

Naumowicz, M., and Figaszewski, Z.A. (2014). The effect of ph on the electrical capacitance of phosphatidylcholine-phosphatidylserine system in bilayer lipid membrane. J. Membr. Biol. 247, 361–369.

Osaki, T., and Takeuchi, S. (2017). Artificial cell membrane systems for biosensing applications. Anal. Chem. 89, 216–231.

Park, B., Yang, H., Ha, T.H., Park, H.S., Oh, S.J., Ryu, Y.-S., Cho, Y., Kim, H.-S., Oh, J., Lee, D.K., et al. (2018). Artificial rod and cone photoreceptors with human-like spectral sensitivities. Adv. Mater. 30, 1706764.

Powers, R.E., Wang, S., Liu, T.Y., and Rapoport, T.A. (2017). Reconstitution of the tubular endoplasmic reticulum network with purified components. Nature 543, 257–260.

Ravula, T., Hardin, N.Z., Ramadugu, S.K., Cox, S.J., and Ramamoorthy, A. (2017). Formation of pH-resistant monodispersed polymer-lipid nanodiscs. Angew. Chem. Int. Ed. 57, 1342–1345.

Ruban, A.V., and Johnson, M.P. (2015). Visualizing the dynamic structure of the plant photosynthetic membrane. Nat. Plants 1, 15161.

Shi, Z., and Baumgart, T. (2015). Membrane tension and peripheral protein density mediate membrane shape transitions. Nat. Commun. 6, 5974.

Shimoni, E., Rav-Hon, O., Ohad, I., Brumfeld, V., and Reich, Z. (2005). Three-dimensional organization of higher-plant chloroplast thylakoid membranes revealed by electron tomography. Plant Cell 17, 2580–2586.

Tachikawa, M., and Mochizuki, A. (2017). Golgi apparatus self-organizes into the characteristic shape via postmitotic reassembly dynamics. Proc. Natl. Acad. Sci. U S A 114, 5177–5182.

Tayebi, L., Ma, Y., Vashaee, D., Chen, G., Sinha, S.K., and Parikh, A.N. (2012). Long-range interlayer alignment of intralayer domains in stacked lipid bilayers. Nat. Mater. 11, 1074–1080.

Terasaki, M., Shemesh, T., Kasthuri, N., Klemm, R.W., Schalek, R., Hayworth, K.J., Hand, A.R., Yankova, M., Huber, G., Lichtman, J.W., et al. (2013). Stacked endoplasmic reticulum sheets are connected by helicoidal membrane motifs. Cell 154, 285–296.

van Meer, G., Voelker, D.R., and Feigenson, G.W. (2008). Membrane lipids: where they are and how they behave. Nat. Rev. Mol. Cell Biol. 9, 112–124.

Vanegas, J.M., Faller, R., and Longo, M.L. (2010). Influence of ethanol on lipid/sterol membranes: phase diagram construction from AFM imaging. Langmuir 26, 10415–10418.

Wang, S., Powers, R.E., Gold, V.A., and Rapoport, T.A. (2018). The ER morphology-regulating lunapark protein induces the formation of stacked bilayer discs. Life Sci. Alli. 1, e201700014.

Yang, P.-W., Lin, T.-L., Hu, Y., and Jeng, U.-S. (2014). Formation of divalent ion mediated anionic disc bicelle–DNA complexes. Soft Matter 10, 2313–2319.

Zhang, M., Huang, R., Ackermann, R., Im, S.C., Waskell, L., Schwendeman, A., and Ramamoorthy, A. (2016). Reconstitution of the Cytb5-CytP450 complex in nanodiscs for structural studies using NMR spectroscopy. Angew. Chem. Int. Ed. 55, 4497–4499.

Zhang, Z., Yang, Y., Pincet, F., Llaguno, M.C., and Lin, C.X. (2017). Placing and shaping liposomes with reconfigurable DNA nanocages. Nat. Chem. 9, 653–659.

Zong, W., Ma, S., Zhang, X., Wang, X., Li, Q., and Han, X. (2017). A fissionable artificial eukaryote-like cell model. J. Am. Chem. Soc. 139, 9955–9960.

Supplemental Information

Self-Assembled Rough Endoplasmic

Reticulum-Like Proto-Organelles

Qingchuan Li and Xiaojun Han

Supplemental Data Items
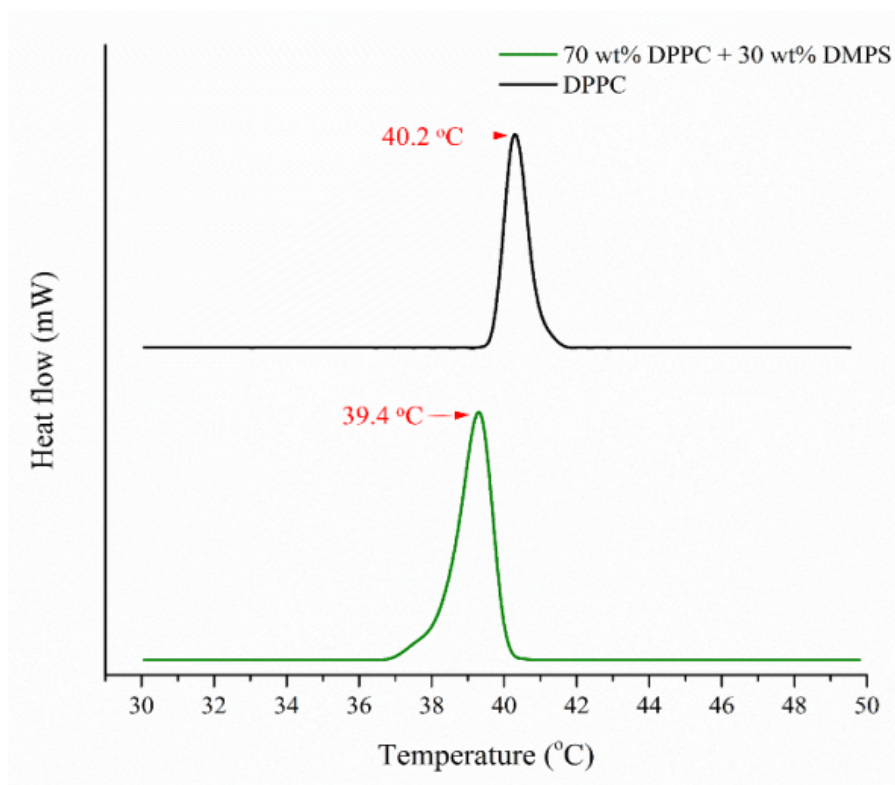
Figure S1. Endothermic calorimetric thermogram, related to Figure 1
Endothermic calorimetric thermogram of stacked bicelles formed from DPPC and DPPC/DMPS (7/3, *w/w*) mixtures. The stacked bicelles were formed in solution with lipid concentration of 0.10 mg/mL and ethanol volume percentage of 50%.
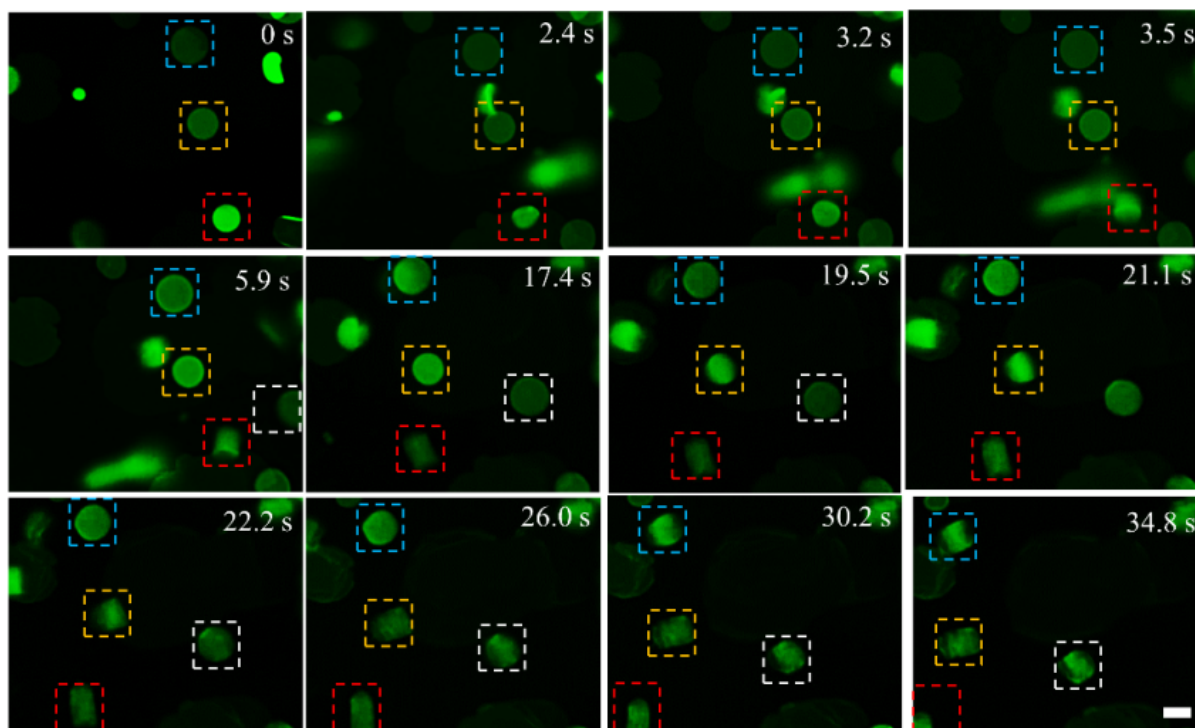
**Figure S2. Fluorescence images with time, related to Figure 1**
Fluorescence images for the transformation process from stacked bicelles to cisternae stacks. The dash boxes with different colors represent different samples. The scale bar was 10 μm.
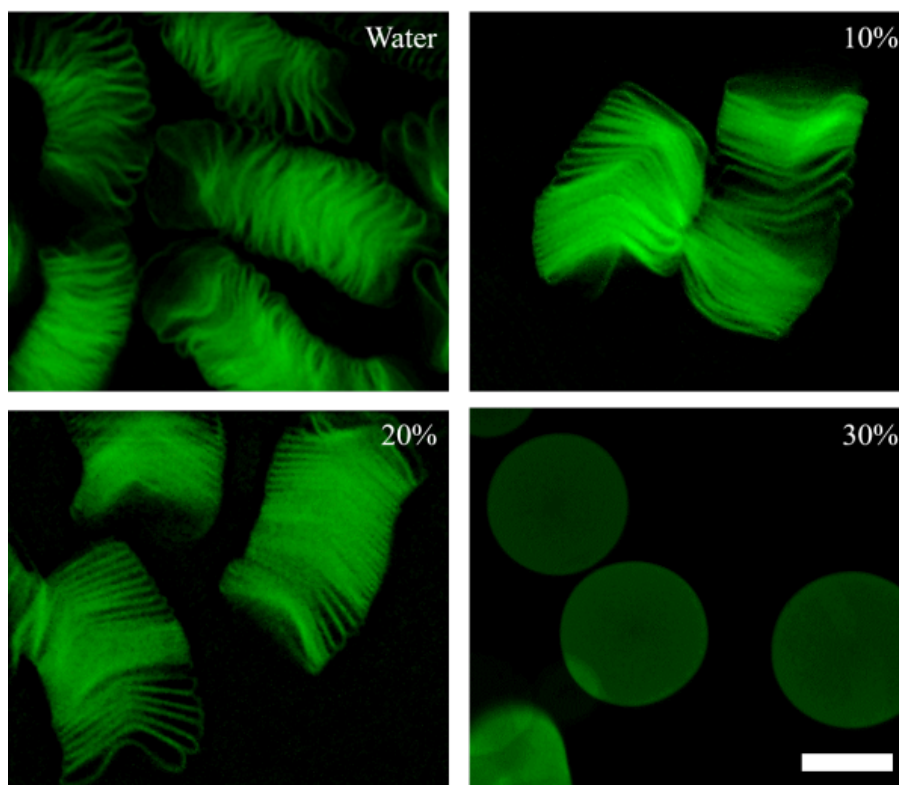
Figure S3. Fluorescence images, related to Figure 1
Fluorescence images of the samples after the stacked bicelles were dispersed into ethanol-water solution with different ethanol volume percentage. The stacked bicelles were formed in 50% ethanol solution from DPPC/DMPS (7/3, w/w). The scale bar was 10 μm.
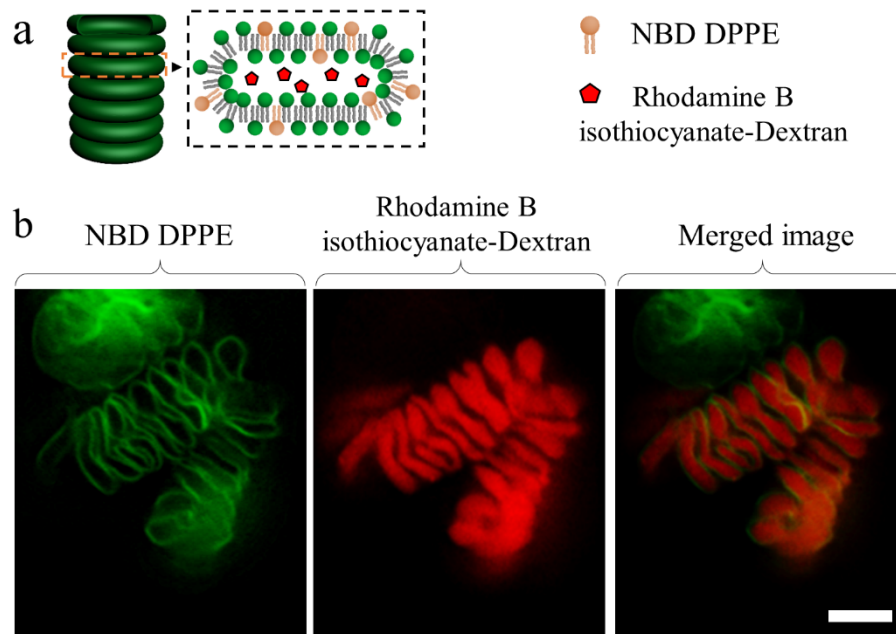
Figure S4. The entrapment of water-soluble fluorescent markers in cisternae stacks during the reorganization process, related to Figure 1

a, Schematic illustration of the entrapment experiments. b, Fluorescence images of the cisternae stacks indicating the encapsulation of fluorescent molecules (red) in the stacks (green). The scale bar was 10 μm.
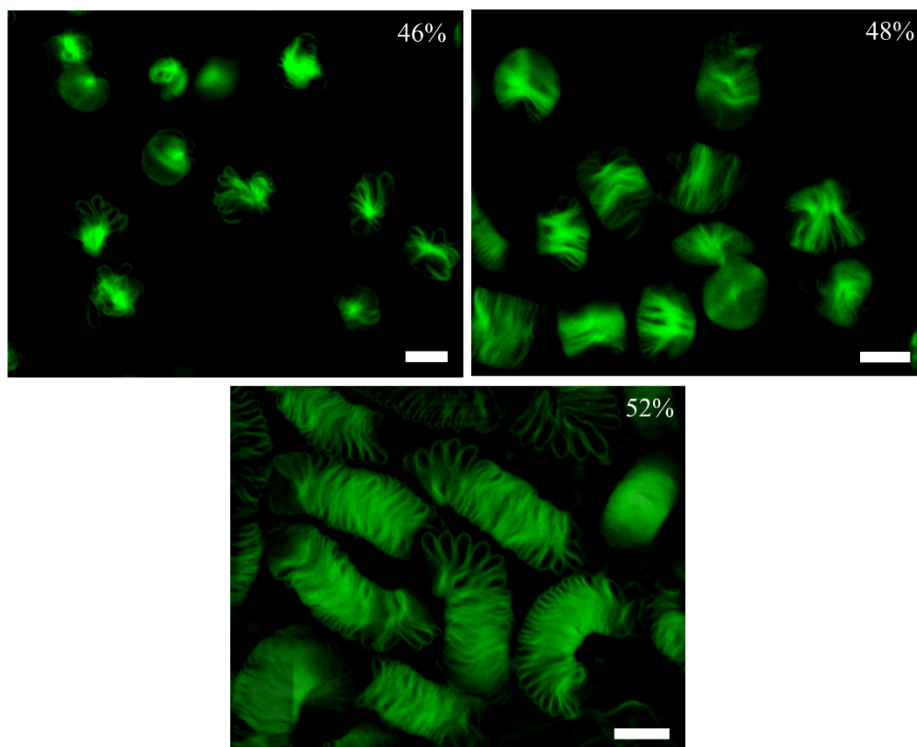
Figure S5. Fluorescence images, related to Figure 1
Fluorescence images of cisternae stacks in water transformed from stacked bicelles formed in different $\Phi_{ethanol}$. The scale bars were 10 μm.
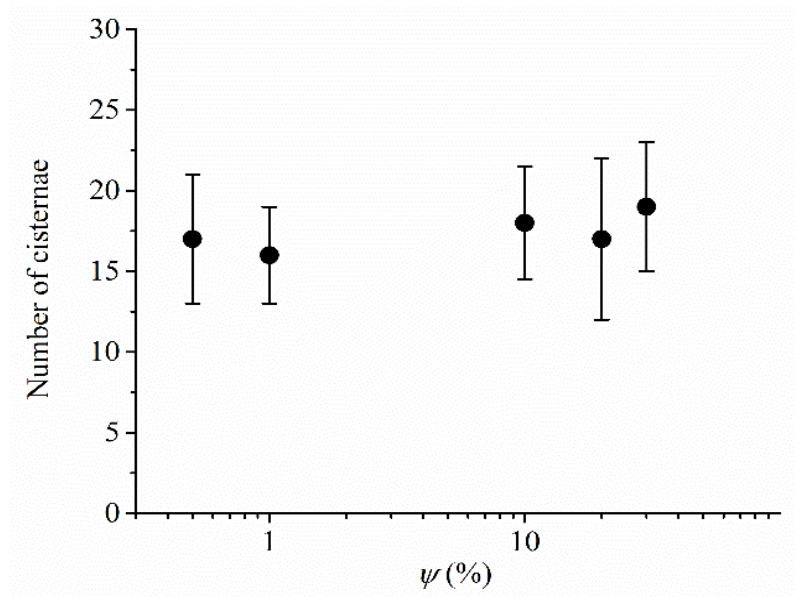
Figure S6. The number of cisternae in single stacks, related to Figure 1
Influence of the percentage of negatively charged DMPS ψ in stacked bicelles on the number of cisternae in the cisternae stacks. The stacked bicelles were formed in solution with lipid concentration of 0.10 mg/mL and ethanol volume percentage of 50%. Error bars are ±SEM.
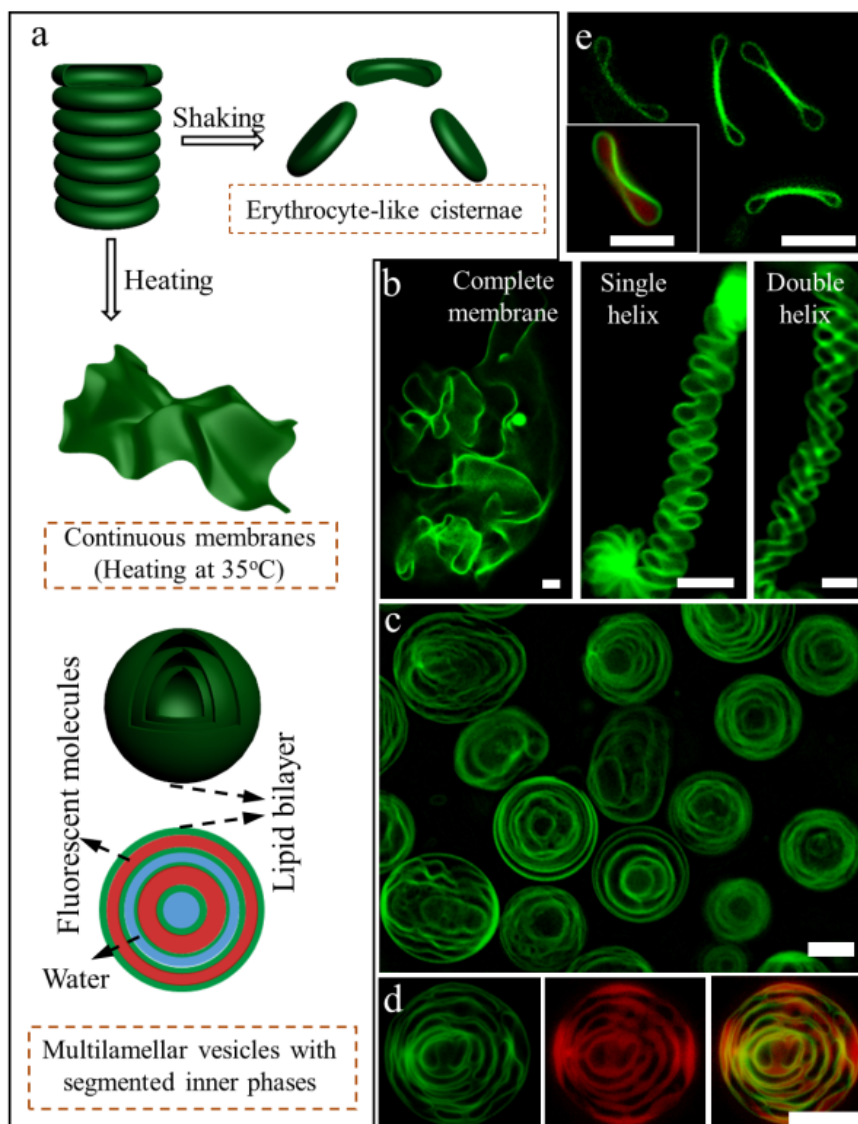
Figure S7. Morphology evolution of cisternae stacks, related to Figure 2

a, Schematic presentation of the morphology evolution of cisternae stacks treated with shaking or heating. b, Fluorescence image of the continuous membrane structures from cisternae stacks by heating the samples at 35ºC for 12h. c, Fluorescence image of multilamellar vesicles formed by heating the cisternae stacks samples at 45ºC. d, Fluorescence images of the multilamellar vesicles with spatially segmented inner phases. e, Fluorescence image of the erythrocyte-like separate cisternae formed by the vigorously shaking of the cisternae stacks samples. The inset in e is the fluorescence image of one cisterna encapsulated with Rhodamine B isothiocyanate-Dextran (~70 kDa). The scale bars were 10 μm. When heating at 45ºC (above T_m), the cisternae stacks quickly transformed to multilamellar vesicles (Fig. S7c). Rhodamine B isothiocyanate-Dextrans (~70 kDa) added during the transformation can be encapsulated to form multilamellar vesicles with spatially segmented inner phases, namely, the contents followed the repeated pattern with water/Dextran in the segments (Fig. S7d). Vigorously shaking would break the cisternae stacks into separate cisternae with similar morphology to erythrocytes (Fig. S7e). During this process, Rhodamine B isothiocyanate-Dextrans can enter the cisternae and be encapsulated (The inset in Fig. S7e).
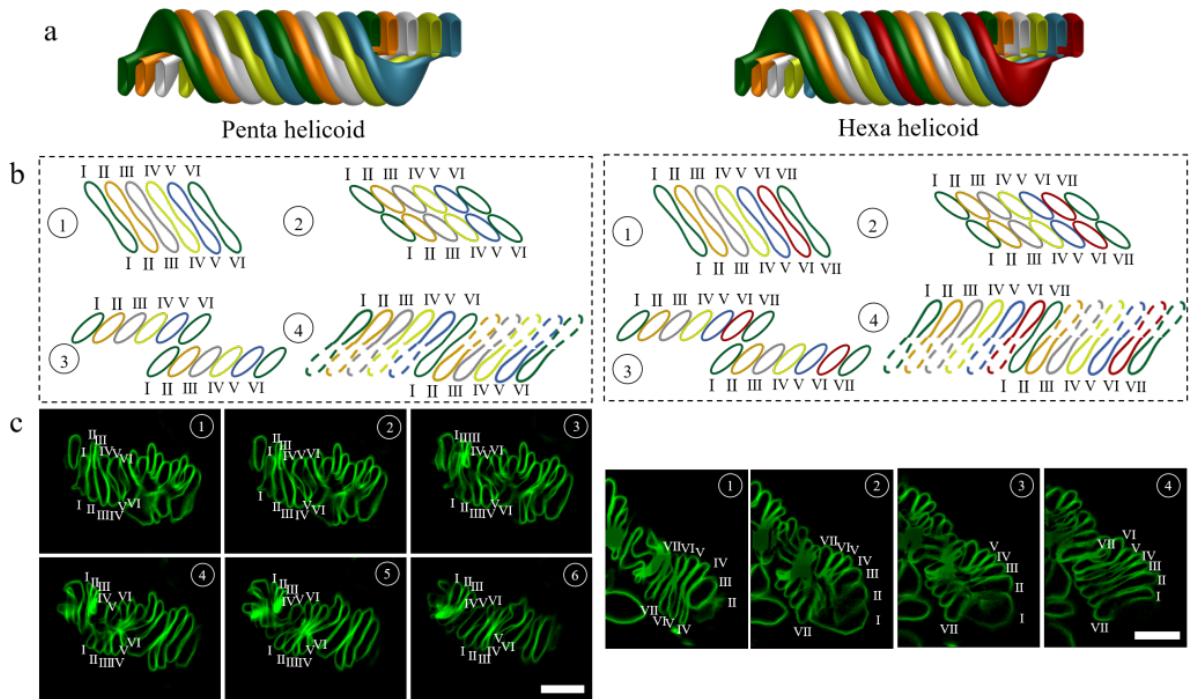
Figure S8. Formation of multiple helicoidal cisternae stacks with *n*=5 and *n*=6, related to Figure 3

a, Schematic representation of penta and hexa helicoidal cisternae stacks. b, Schematic illustration of the variation tendency of the cisternae stacks in Z-stacks under laser confocal fluorescence microscope for cisternae stacks with *n*=5 (left) and *n*=6 (right). c, Typical fluorescence images of the cisternae stacks with multiple helicoidal morphologies visualized in Z-stacks by laser confocal microscope: *n*=5 (left) and *n*=6 (right). The scale bars were 10 μm.
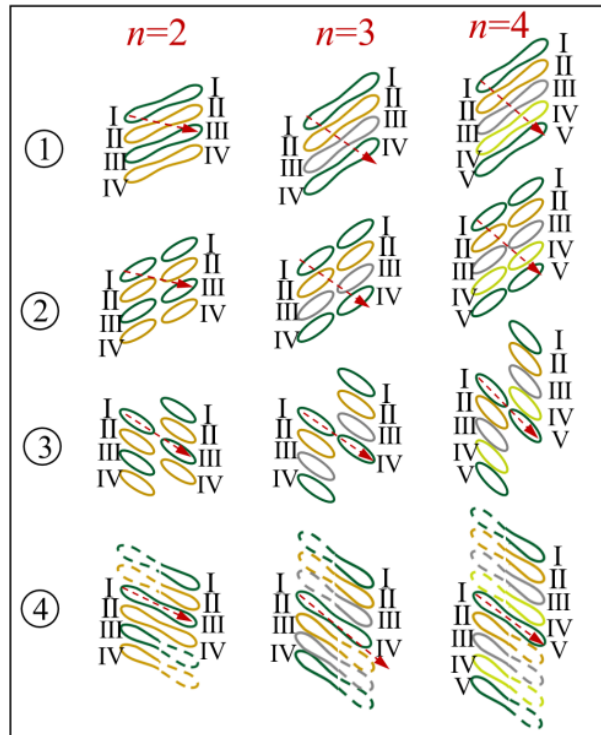
Figure S9. Schematic illustration, related to Figure 3
Schematic illustration of variation of the cisternae in Z-stacks under laser confocal fluorescence microscope for cisternae stacks with different number of helicoid n. Different color represented the cisternae from different helicoid in the multiple helicoidal cisternae stack. The dashed red arrows indicated the connection between cisternae.
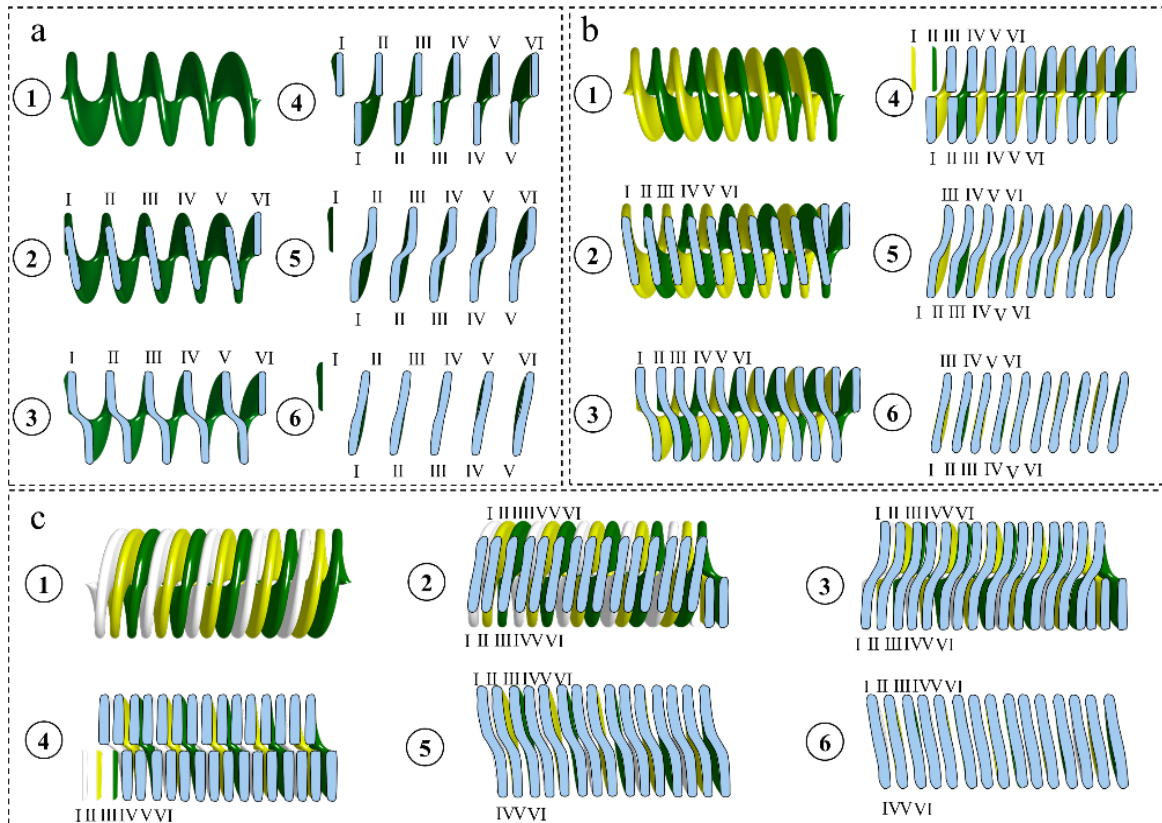
Figure S10. Serial sections, related to Figure 3

Serial sections of helicoidal models with different number of helicoid: (a) *n*=1, (b) *n*=2, (c) *n*=3.
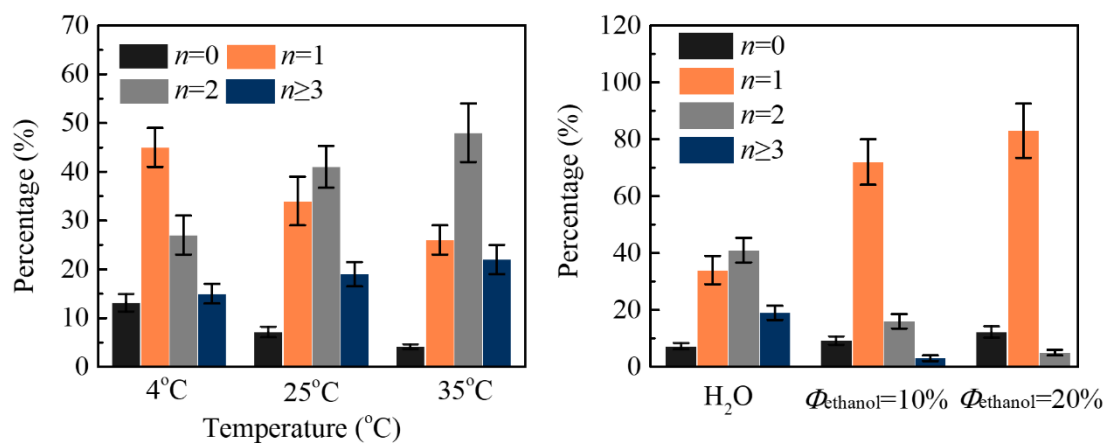
Figure S11. Statistical analysis, related to Figure 3

Influence of temperature (a) and solvent (b) conditions for the reorganization of DPPC/DMPS (7/3, *w/w*) bicelles to cisternae stacks on the percentages of helicoidal structures with different *n* in the samples. The stacked bicelles were formed in 50% ethanol solution. Error bars are ±SEM.
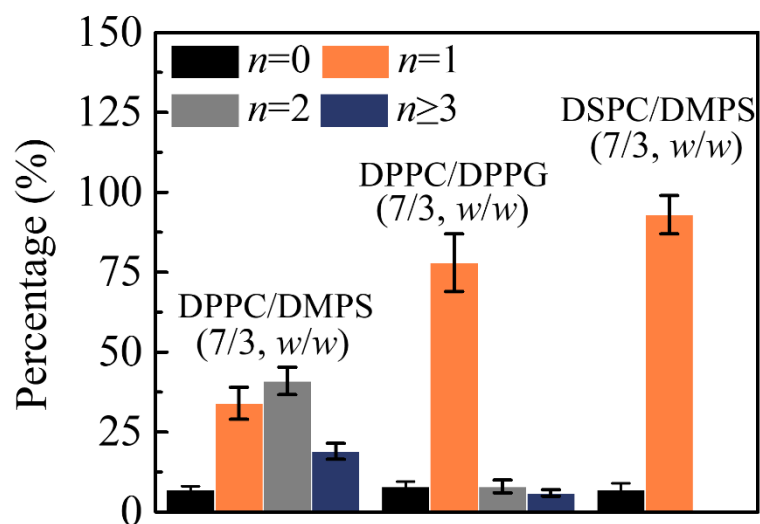
Figure S12. Statistical analysis, related to Figure 3
Influence of lipid compositions on the formation of helicoidal cisternae stacks with different n
(N=100). Error bars are ±SEM.
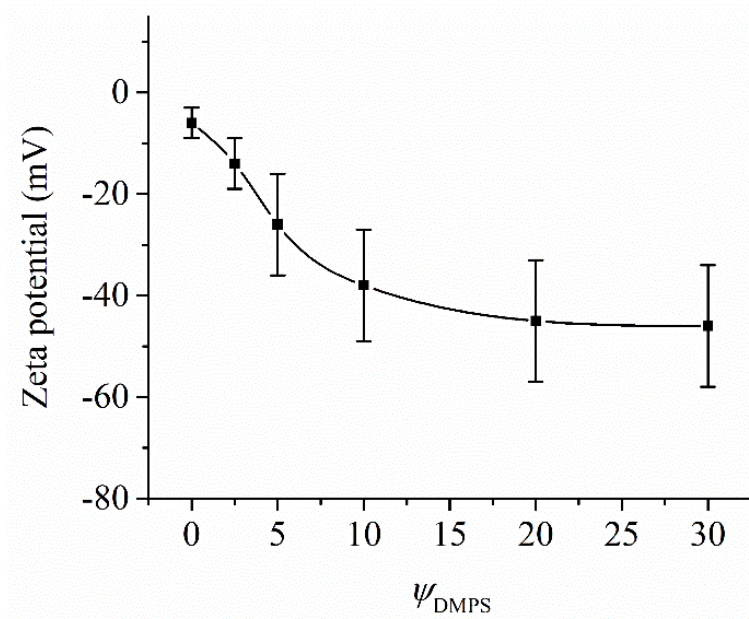
Figure S13. Influence of DMPS on the Zeta potential of helicoids, related to Figure 3
Variation of zeta potential of cisternae stacks in water with ψ_{DMPS}. Error bars are ±SEM.
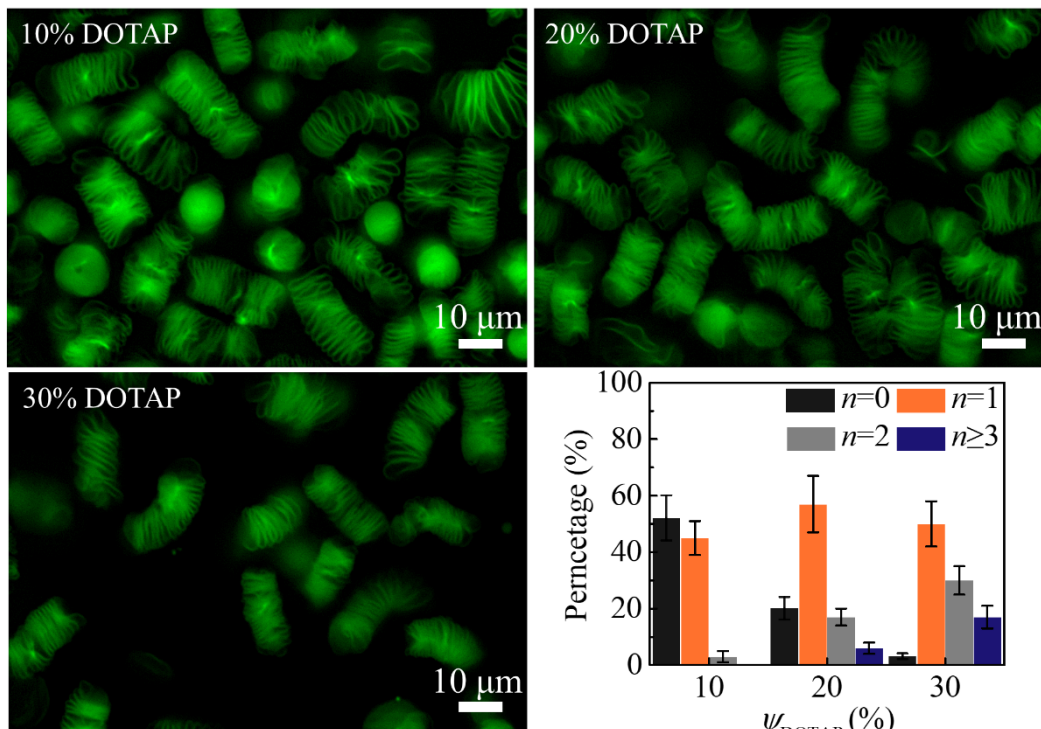
Figure S14. Fluorescence images and statistical analysis, related to Figure 3
Fluorescence images of DPPC/DOTAP cisternae stacks incorporated different percentages of DOTAP, and counted percentages of cisternae stacks with different n in the samples. Error bars are ±SEM. The scale bars were 10 μm.
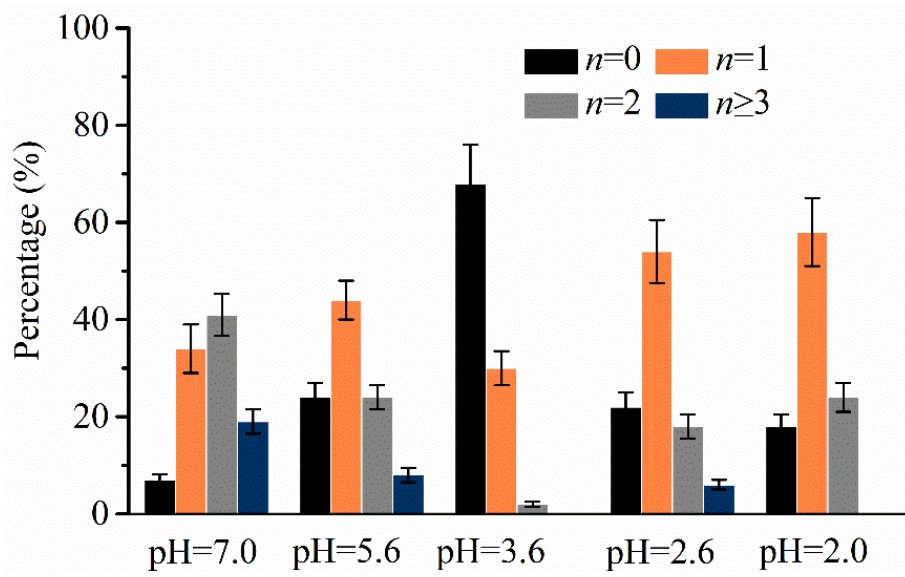
Figure S15. Influence of pH on the morphologies of lipid assemblies, related to Figure 3
Variation of the percentages of different morphologies in cisternae stacks with solution pH value.
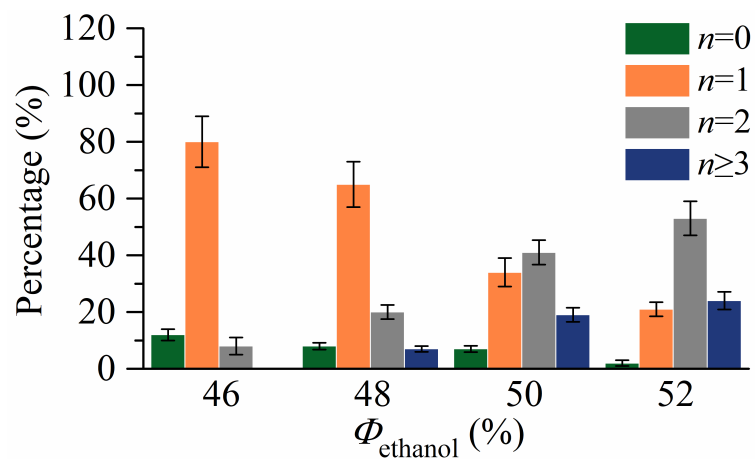Error bars are ±SEM.

Figure S16. Statistical analysis, related to Figure 3

Influence of ethanol volume percentage $\Phi_{ethanol}$ for the formation of DPPC/DMPS (7/3, w/w) stacked bicelles on the percentages of cisternae stacks with diffetent n (N=200). Error bars are ±SEM.
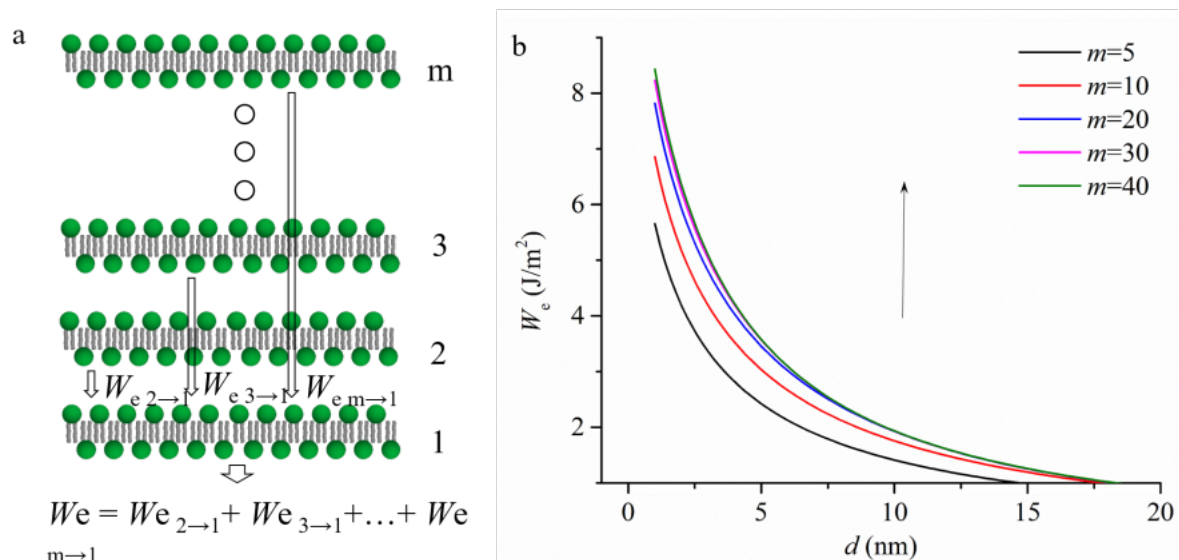
Figure S17. Interlayer energy calculation, related to Figure 3

The accumulation of electrostatic repulsive energy in the stacked bicelles with m lipid bilayers when they were dispersed in water. a, Schematic illustration of the accumulation of electrostatic repulsive energy on one lipid bilayer from other lipid bilayers in stacked bicelles. b, Calculated electrostatic repulsive energy W_e with m.
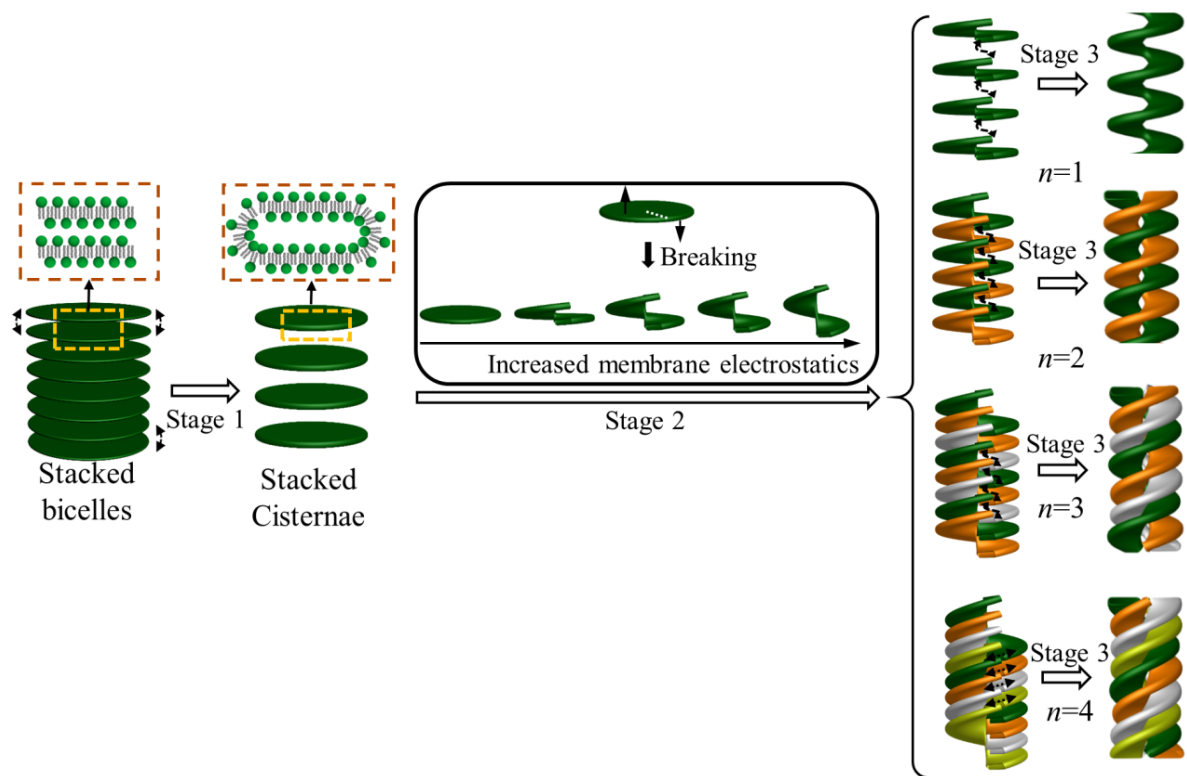
Figure S18. Schematic illustration, related to Figure 3
Schematic illustration for the reorganization of stacked bicelles to helicoidal cisternae stacks with different n.
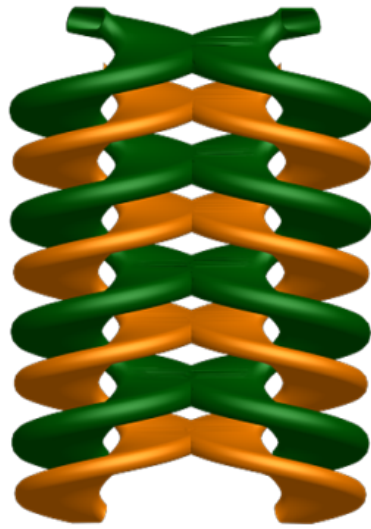
Figure S19. Anticipated membrane structures in RER, related to Figure 3
Schematic representation of double helicoidal model that might exist in natural RER.
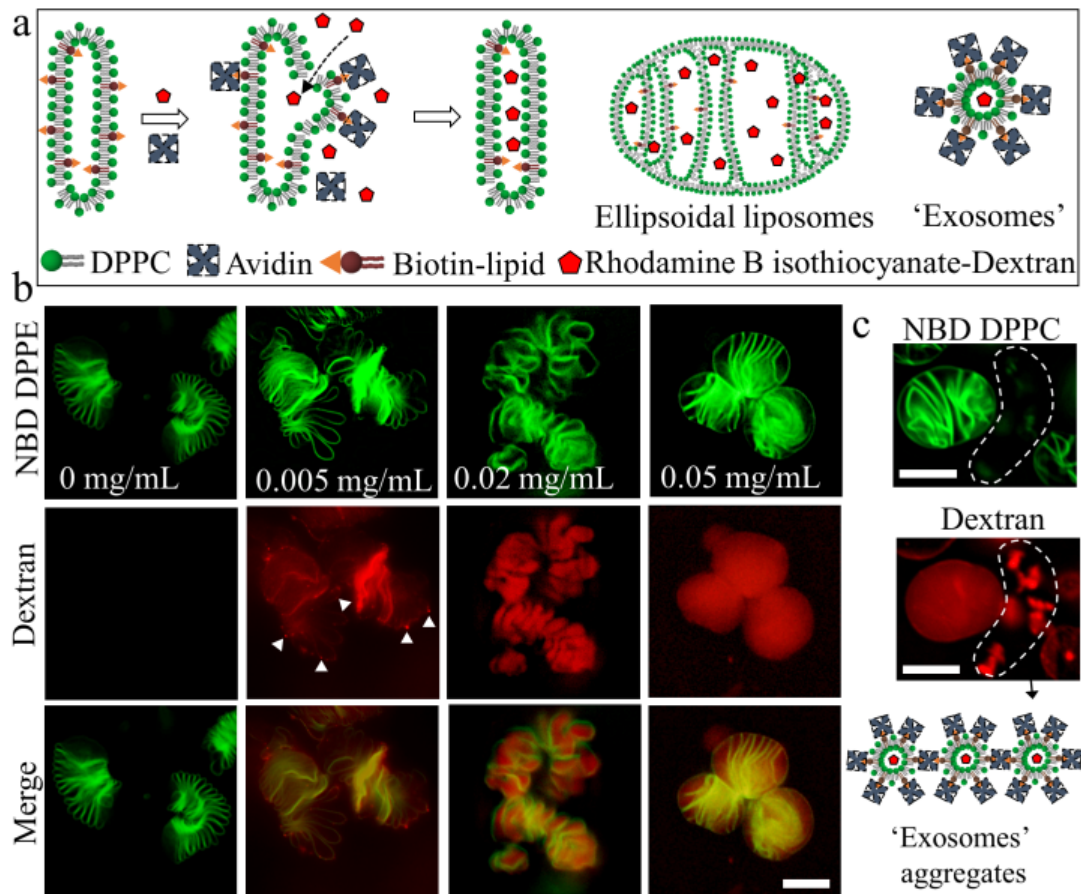
Figure S20. Loading of fluorescent molecules in the RER-like cisternae stacks, related to Figure 4

a, Schematic illustration of the entrapment of fluorescent molecules through the exocytosis-like process caused by the binding of avidin to cisternae stacks incorporated with Biotinyl Cap PE. b, Fluorescence images of samples composed of DPPC/DMPS/ Biotinyl Cap PE (*w/w/w*, 7/2/1) after incubating with avidin of different concentrations. The white arrow heads indicated the formation of liposomes on the membrane surface. c, Fluorescence images and schematic illustration for the formation of 'exosome' aggregates in solutions. The concentration of Rhodamine B isothiocyanate-Dextran (~70 kDa) was 0.01 mg/mL. The incubation time was fixed at 2h. The scale bars were 10 μm.
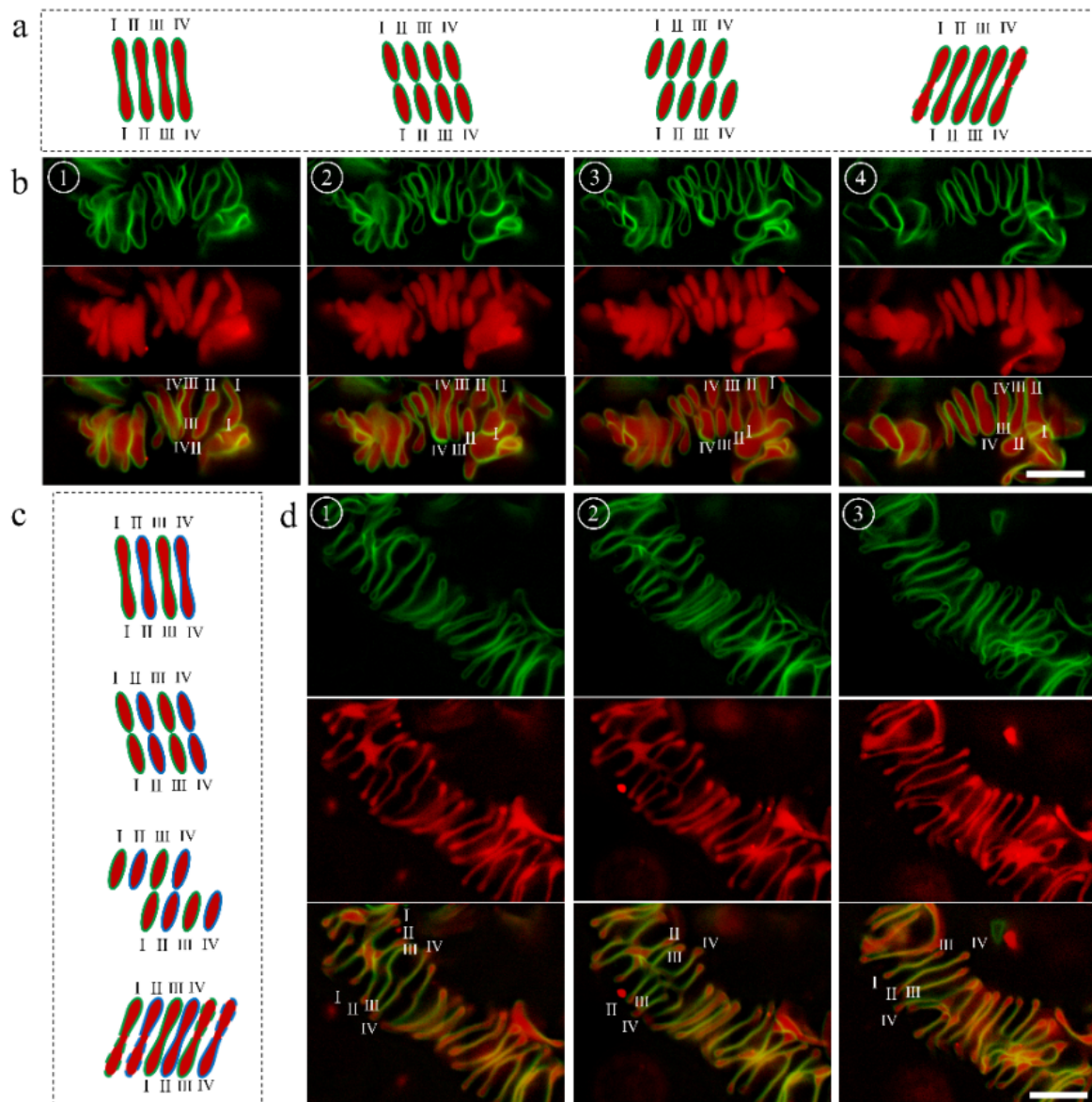
Figure S21. **Confirmation of the helicoidal structures after encapsulating Rhodamine B isothiocyanate-Dextran (~70 kDa), related to Figure 4**

a, Schematic illustration of the variation tendency of the RER-like helicoidal cisternae stacks in Z-stacks. b, Typical fluorescence images the RER-like cisternae stacks (green) encapsulated with fluorescent molecules (red) visualized in Z-stacks. c, Schematic illustration of the variation tendency of the double helicoidal cisternae stacks in Z-stacks. d, Typical fluorescence images the double helicoidal cisternae stacks (green) encapsulated with fluorescent molecules (red) visualized in Z-stacks. The Morphology of the cisternae stacks were determined according to Fig. S9 as labelled in Fig. S21b, d. The scale bars were 10 μm.
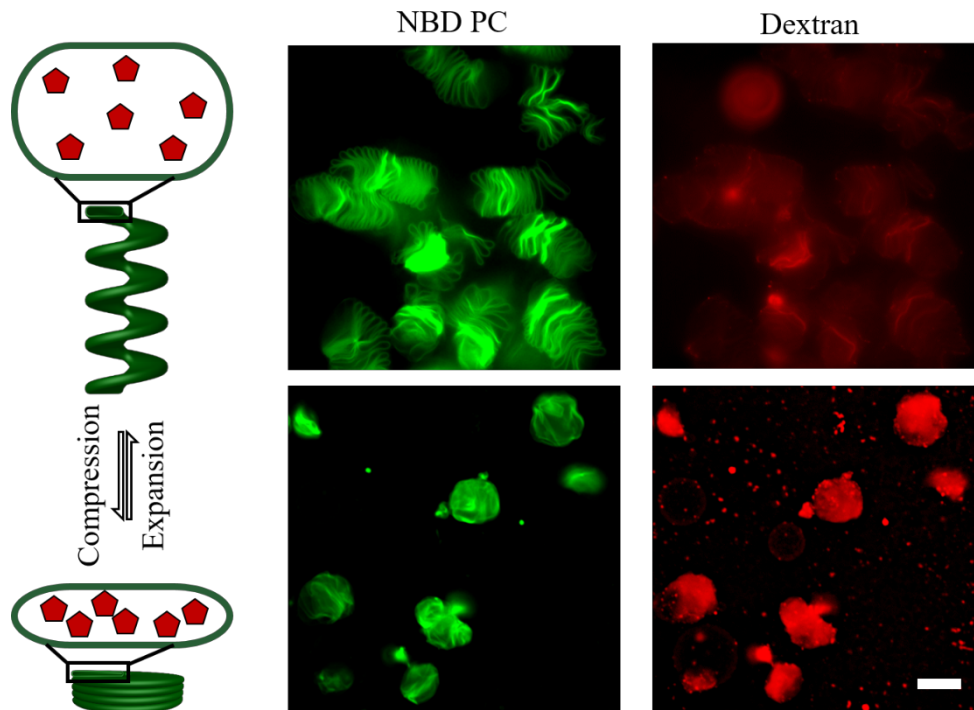
NBD PC   Dextran

Figure S22. "Breathing" cisternae stacks, related to Figure 4
Schematic illustration of "breathing" process of helicoidal cisternae stacks to realize the reversible concentration and dilution of dextrans, and typical fluorescence images the expanded cisternae stacks (top) in water and compressed   cisternae stacks (bottom) in 150 mM PBS encapsulated with Rhodamine B isothiocyanate-Dextran (~70 kDa) (red). The scale bar was 10 μm.

Transparent Methods
Experimental Procedures
Materials 1,2-dipalmitoyl-*sn*-glycero-3-phosphocholine (DPPC), 1,2-distearoyl-*sn*-glycero-3 -phosphocholine (DSPC), 1,2-dimyristoyl-*sn*-glycero-3-phospho-L-serine (sodium salt) (DMPS), 1,2-dipalmitoyl-*sn*-glycero-3-phospho-(1'-*rac*-glycerol) (sodium salt) (DPPG), 1,2-dioleoyl -3-trimethylammonium-propane (chloride salt) (DOTAP), 1,2-dipalmitoyl-sn-glycero-3 -phosphoethanolamine-N-(cap biotinyl) (sodium salt) (16:0 Biotinyl Cap PE), 1-Myristoyl-2-[12-[(7-nitro-2-1,3-benzoxadiazol-4-yl)amino]dodecanoyl]-*sn*-Glycero-3-Phosphocholine (NBD PC) were purchased from Avanti Polar Lipids (USA). Texas red labelled 1,2-dihexadecanoyl-*sn*-glycero-3-phosphoethanolamine, triethylammonium salt (TR-DHPE) was obtained from Invitrogen (China). Avidin from egg white, peroxidase from horseradish (HRP), Amplex Red, hydrogen peroxide, fluorescein isothiocyanate (FITC)-labelled dextrans (150 kDa), Rhodamine B isothiocyanate-Dextran (70 kDa), ethanol, sodium chloride, magnesium chloride, disodium hydrogen phosphate, and sodium dihydrogen phosphate were purchased from Sigma (China). Millipore Milli-Q water with a resistivity of 18.2 MΩ cm was used in the experiment.

Formation of microsized stacked bicelles incorporated with charged lipids. Stacked bicelles were prepared according to our previously described procedure with little modification(27). Briefly, 10 μL of lipid solution (5.0 mg/mL in ethanol) was placed in a centrifuge tube and dried under N_2 stream. Then the lipids were re-dissolved in ethanol (V_1) and water (V_2) mixture solution (V_1+V_2=500 μL). Afterwards, the mixture was sealed in a cell with thickness of 1.5 cm. The temperature of the cell was controlled with a Linkam PE120 heat stage: 50°C for 30min, and slow decrease to 25°C at a rate of 0.5°C/min. To form stacked bicelles in different ethanol volume percentage $\Phi_{ethanol}$, the ratio of V_1 to V_2 was modulated. To form stacked bicelles incorporated with charged lipids, the composition of the lipid solution was varied with fixed lipid concentration of 0.10 mg/mL. 1.0% NBD PC or 0.5% TR-DHPE was labelled in the cisternae stacks for the observation under microscope.

Formation of helicoidal cisternae stacks from stacked bicelles. Helicoidal cisternae stacks were formed from stacked bicelles by replacing the solvent with pure water or ethanol-water solution with different $\Phi_{ethanol}$. To investigate the influence of solvent temperature, water with temperature of 4°C, 25°C, and 35°C were respectively used for helicoidal cisternae stacks formation. To trap fluorescent molecules in the cisternae stacks during the reorganization process, water solution containing 0.01 mg/mL Rhodamine B isothiocyanate-Dextran (~70 kDa) was used for helicoidal cisternae stacks formation. To investigate their morphology evolution, the helicoidal cisternae stacks were treated with heating or shaking in solution containing Rhodamine B isothiocyanate-Dextran (~70 kDa).

Molecules loading and enzyme catalytic reactions in the helicoidal cisternae stacks. For the efficient loading of molecules, helicoidal cisternae stacks composed of DPPC/DMPS/ Biotinyl Cap PE (*w/w/w*, 7/2/1) were formed through the reorganization of stacked bicelles. Rhodamine B isothiocyanate-Dextran molecules were encapsulated by incubating the cisternae stacks containing Biotinyl Cap PE with different concentrations of avidin for 2h. To control the reversible compression and expansion of the cisternae stacks encapsulated with fluorescent molecules, the cisternae stacks were reversibly dispersed in PBS for compression and water for expansion. A microreactor based on the 'breathing' helicoidal cisternae stacks was constructed by incubating the cisternae stacks in 0.4 U/mL HRP for enzyme encapsulation. The enzyme catalytic reactions were initiated by adding Amplex Red and H_2O_2 in the cisternae stacks dispersion to final concentrations of 100 μM and 40 μM, respectively. The enzyme catalytic reactions in both compressed cisternae stacks and expanded cisternae stacks were performed and compared.

Characterization. Fluorescence images were taken under a fluorescence microscope (Olympus IX73, Japan) and a confocal laser scanning microscope (Olympus FV 3000, Japan). To obtain the 3D morphologies of the helicoidal cisternae stacks, the cisternae stacks were visualized in serial sections, each 0.32 μm thick, by confocal laser scanning microscope. To obtain the 3D morphologies of the helicoidal cisternae stacks formed in NaCl solution, $CaCl_2$ solution, and low pH solution, after the incubation in the above solvent media for 4h, the cisternae stacks were dispersed in water to form loosely packed structures for the better characterization by the confocal laser scanning microscope. The images in Z-stacks were aligned and reconstructed using the software Matlab 2012. DSC experiments were carried out using a Mettler-TOLED DSC3 differential scanning calorimeter. The heating of the stacked bicelles samples was performed in the temperature range 30~50 °C at the scan rate of 1°C/min. To obtain the small angle X-ray scattering measurement result, the stacked bicelles samples were firstly concentrated to ~10 mg/mL via centrifugation. The measurement was performed at 25ºC by a SAXSpace small angle X-ray scattering instrument (Anton Paar, Austria, Cu-Kα, $\lambda = 0.154$ nm).